

Turbulent planar wakes of viscoelastic fluids analysed by direct numerical simulations

Mateus C. Guimarães¹, Fernando T. Pinho^{2,3} and Carlos B. da Silva^{1,†}

¹IDMEC/LAETA, Instituto Superior Técnico, Universidade de Lisboa, 1049-001 Lisboa, Portugal

²CEFT, Faculdade de Engenharia, Universidade do Porto, 4200-465 Porto, Portugal

³ALiCE, Faculdade de Engenharia, Universidade do Porto, 4200-465 Porto, Portugal

(Received 3 November 2021; revised 18 April 2022; accepted 21 June 2022)

Direct numerical simulations employing the finitely extensible nonlinear elastic constitutive model closed with Peterlin's approximation (FENE-P) are used to investigate the far-field region of turbulent planar wakes of viscoelastic fluids and to develop the theory describing these flows. The theoretical results display excellent agreement with the simulations and provide new scaling laws for the evolution of the shear layer thickness $\delta(x) \sim x^{1/2}$, mean velocity deficit $\Delta U(x) \sim x^{-1/2}$ and, for very high Deborah numbers, of the maximum polymer shear stresses $\sigma_c^{[p]}(x) \sim x^{-2}$ and averaged polymer chain extension $\text{tr}(\bar{C}(x) - I) \sim x^{-2}$, where x is the streamwise distance from the solid body generating the wake. The theory is able to show the existence of self-similarity for the profiles of mean velocity, mean polymer shear stress, averaged polymer chain extension and the conditions for similarity of the turbulent shear stress, and is very well supported by the numerical simulations. Similarly to the case of viscoelastic turbulent planar jets (Guimarães *et al.*, *J. Fluid Mech.*, vol. 899, 2020, p. A11), when the inlet Weissenberg and Deborah numbers are sufficiently large, turbulent viscoelastic wakes exhibit a considerable reduction of the spreading rate and of the normalised Reynolds stresses. However, for very large downstream locations the turbulent viscoelastic wake recovers the classical evolution laws observed for Newtonian turbulent planar wakes.

Key words: viscoelasticity, turbulence simulation

1. Introduction

The wake of a solid body immersed in a constant free stream velocity field is a classical problem in fluid mechanics that has attracted the attention of engineers and scientists for many years. For Newtonian fluids the far field region of the wake is of particular interest since it admits the existence of self-similar solutions to the equations of motion,

† Email address for correspondence: carlos.silva@tecnico.ulisboa.pt

and because it provides a characteristic signature of the body which ‘remains’ in the fluid after it has passed through it. For turbulent flows the latter issue is related to the non-universal character of the large-scale eddies, which has been difficult to model; nevertheless the theory of the far-field fully developed turbulent region of turbulent wakes for Newtonian fluids has been established quite some time ago (Schlichting 1930; Tennekes & Lumley 1972; Townsend 1976; Pope 2000). The situation is very different, however, when one considers the far-field region of turbulent wakes with viscoelastic fluids, such as those obtained when a Newtonian solvent carries a small amount of long chain polymer molecules, and presently no theory exists to describe the evolution of these flows.

The majority of the existing numerical and experimental works addressing wakes from bluff bodies with viscoelastic fluids have investigated the instability characteristics of the flow, and a relatively large range of Reynolds numbers has been covered (Gadd 1966; Sarpkaya, Raineyt & Kell 1973; Kato & Mizuno 1983; Cadot & Kumar 2000; Cressman, Bailey & Goldberg 2001; Coelho & Pinho 2003*a,b*, 2004; Richter, Iaccarino & Shaqfeh 2012; Xiong, Bruneau & Kellay 2013). Specifically, these works have addressed: (i) the influence of the fluid elasticity on the vortex shedding frequency; (ii) the base pressure in the solid body; (iii) the drag coefficient; (iv) the formation length of the wake; (v) the emerging vortex structures; and (vi) the critical Reynolds numbers demarcating the transition between different shedding regimes, as described by Williamson (1996) for Newtonian fluids. Non-monotone variations of these quantities with the rheological parameters of the fluid have been found, and different behaviours have been observed depending on the vortex shedding regime. Another feature which seems to be characteristic of wakes from viscoelastic fluids, and that has been observed in the majority of these studies, is the stabilising effect of the viscoelasticity of the fluid on the flow structures, and the concomitant depletion of small-scale vorticity. Similar effects have been observed also (for viscoelastic fluids) in turbulent jets (Guimarães *et al.* 2020), turbulent channel and pipe flows (Kim *et al.* 2007; Horiuti, Matsumoto & Fujiwara 2013) and isotropic turbulence (Perlekar, Mitra & Pandit 2010; Ferreira, da Silva & Pinho 2016).

Until now only a relatively few works investigated the far-field turbulent wake region from bluff bodies with viscoelastic fluids. Pokryvailo *et al.* (1973) showed, using laser Doppler anemometer measurements, that the decay rate of the velocity defect in the near field region of the flow behind disks and spheres, is smaller for viscoelastic fluids than in the classical (Newtonian) case. Using pictures obtained with tracers, Borisov *et al.* (1990) observed a decrease in all the components of turbulent velocity fluctuations for viscoelastic fluids compared with the reference (Newtonian) case, which amounts to a factor of two in the wake behind a falling ellipsoid, and by a factor of 30% for the wake behind a falling cup. However, the shape of the normalised mean velocity profiles was found to be unaffected by the presence of polymers. Pinho & Whitelaw (1991) also observed considerably smaller values of turbulent velocity fluctuations in the wake region close to a confined baffle for polymer solutions compared with the Newtonian case, when the concentration of polymers in the solution was increased above a given threshold. Finally, Cressman *et al.* (2001) investigated two-dimensional (2-D) cylinder wakes using laser Doppler anemometer and observed a dramatic decrease of the transverse velocity fluctuations for the viscoelastic case, compared with the Newtonian reference case, when the molecular weight of the polymer additive within the Newtonian solvent is sufficiently large.

In the present work we perform several direct numerical simulations (DNS) of spatially evolving turbulent planar wakes with dilute polymer solutions, described by the finitely extensible nonlinear elastic constitutive equation closed with the Peterlin approximation

(FENE-P), in order to develop a theory for the far-field fully developed turbulent region of the flow. The new theory draws from theoretical models originally developed for viscoelastic turbulent planar jets as described in Guimarães *et al.* (2020), however, the present planar wake simulations have a substantially larger computational domain, extending up to 84 times the initial body length in the streamwise direction, compared with 18 times the inlet slot-width used in the DNS of turbulent viscoelastic jets in Guimarães *et al.* (2020), and to 27 times the inlet slot-width discussed in the additional case presented at the Appendix of that paper. This allows one to clearly observe for the first time the recovery of the Newtonian evolution laws in the distant far-field region of the wake, where the local Deborah and Weissenberg numbers have decayed considerably, as anticipated by Guimarães *et al.* (2020) for the case of the turbulent viscoelastic jet. This occurs because, as in the case of the turbulent jet, the local Deborah and Weissenberg numbers are decreasing functions of the distance x , and the observed viscoelastic effects cease for very large streamwise distances x . For this reason the turbulent far-field region of the viscoelastic wake has to be divided into two regions: (i) a far-field region where viscoelastic effects are present; and (ii) a distant far-field region where viscoelastic effects vanish.

This paper is organised as follows. In § 2 we present the governing equations, numerical methods and the physical and computational parameters used in the DNS of viscoelastic turbulent planar wakes carried out in the present work. Section 3 describes the main flow features of turbulent viscoelastic wakes, focusing in the far-field region and using a reference Newtonian DNS and the theory of classical (Newtonian) turbulent planar wakes. In § 4 a theory describing the far field of turbulent viscoelastic wakes is proposed and assessed using the new DNS data. Section 5 concludes the work with an overview of the main results and conclusions.

2. Direct numerical simulations of turbulent viscoelastic wakes

This section describes the governing equations, numerical methods and the physical and computational parameters of all the simulations carried out in the present work.

2.1. The FENE-P fluid equations

To characterise the rheology of dilute polymer solutions we use the FENE-P model proposed by Bird, Dotson & Johnson (1980). The momentum equation is given by

$$\frac{\partial \mathbf{u}}{\partial t} + \mathbf{u} \cdot \nabla \mathbf{u} = -\frac{1}{\rho} \nabla p + \nu^{[s]} \nabla^2 \mathbf{u} + \frac{1}{\rho} \nabla \cdot \boldsymbol{\sigma}^{[p]}, \quad (2.1)$$

where \mathbf{u} is the velocity field, ρ the solvent density, p the pressure, $\nu^{[s]}$ the (Newtonian) solvent kinematic viscosity and $\boldsymbol{\sigma}^{[p]}$ is the polymer stress tensor, which is calculated as

$$\boldsymbol{\sigma}^{[p]} = \frac{\rho \nu^{[p]}}{\tau_p} [f(C_{kk}) \mathbf{C} - \mathbf{I}], \quad (2.2)$$

where $\nu^{[p]}$ is the zero-shear-rate kinematic viscosity of the solution, τ_p is the maximum relaxation time of the polymer chains, \mathbf{I} is the identity matrix, $f(C_{kk}) \equiv (L^2 - 3)/(L^2 - C_{kk})$ is the Peterlin function and \mathbf{C} is the conformation tensor. The model parameter L^2 is the square of the maximum extensibility of the polymer molecules normalised by their equilibrium radius $\langle R^2 \rangle_0$ (the brackets denote an ensemble average over all configurations

of the chain) and the conformation tensor is by definition the normalised covariance matrix of the polymer chain end-to-end vector \mathbf{r} , i.e. $\mathbf{C} \equiv \langle \mathbf{r}'\mathbf{r}' \rangle / \langle R^2 \rangle_0$. The conformation tensor \mathbf{C} is governed by the following evolution equation:

$$\frac{\partial \mathbf{C}}{\partial t} + \mathbf{u} \cdot \nabla \mathbf{C} = \nabla \mathbf{u}^T \cdot \mathbf{C} + \mathbf{C} \cdot \nabla \mathbf{u} - \frac{1}{\tau_p} [f(C_{kk})\mathbf{C} - \mathbf{I}], \quad (2.3)$$

where the first two terms on the right-hand side of (2.3) represent the elongation of the polymer chains caused by the velocity gradients (polymer stretching/distortion term) and the last term represents the potential elastic energy stored in the polymers (relaxation term). Finally, the fluid incompressibility condition is imposed by the continuity equation

$$\nabla \cdot \mathbf{u} = 0, \quad (2.4)$$

which closes the set of equations to be solved in the numerical simulations.

2.2. Numerical methods

In the present work the momentum equation is solved with a highly accurate code using pseudospectral/‘compact’ finite difference schemes, that has been used in several previous works (see da Silva, Lopes & Raman (2015), Guimarães *et al.* (2020) and references therein). The streamwise (x) derivatives are computed with a sixth-order ‘compact’ scheme (Lele 1992) while the derivatives in the normal (y) and spanwise (z) directions are computed using pseudospectral methods (Canuto *et al.* 1987), where dealiasing is performed with the 2/3rd rule. Temporal advancement is computed with an explicit third-order low storage Runge–Kutta time-stepping scheme (Williamson 1980) and pressure–velocity coupling is ensured by a fractional step method (Kim & Moin 1985).

Inflow and outflow boundary conditions are imposed in the boundaries facing the streamwise direction, with a prescribed inlet mean velocity profile superimposed to a random velocity fluctuation with an energy spectrum characteristic of isotropic turbulence, and non-reflective outflow boundary conditions at the outlet boundary (Orlanski 1976).

The stretching term in the evolution equation of the conformation tensor field is calculated with central second-order finite differences, and the convection term is calculated with the shock-capturing scheme of Kurganov & Tadmor (2000). Cell area-averaged velocities are obtained as in Guimarães *et al.* (2020), while time advancement is performed with the same third-order explicit Runge–Kutta scheme used for the velocity update and no use is made of any artificial numerical diffusion. As in Guimarães *et al.* (2020), we monitored the values of the conformation tensor field for all points of the computational grid and checked that the symmetric positive-definiteness character of \mathbf{C} was maintained for all time iterations, as well as the six conditions imposed by the Cauchy–Schwartz inequality, e.g. $-\sqrt{|C_{11}^\pm C_{22}^\pm|} \leq C_{12}^\pm \leq \sqrt{|C_{11}^\pm C_{22}^\pm|}$.

In the present work we use the same numerical code employed in Guimarães *et al.* (2020) with a slight modification, for reasons of computational cost. In Guimarães *et al.* (2020) the method of Vaithianathan *et al.* (2006) is used to calculate the convection term of the conformation tensor equation, which can yield first- or second-order accuracy to the approximation of $\mathbf{u} \cdot \nabla \mathbf{C}$, depending on which option maximises some eigenvalues of \mathbf{C} (see Guimarães *et al.* (2020) for details). This method is based on the work of Kurganov & Tadmor (2000) and it is designed to reduce the order of the approximation used in the computation of the convection term of the conformation tensor equation into first order, only at locations where shocks (discontinuities) arise in the conformation

Wi	τ_p	Re_λ	A_δ	$A_{\Delta U}$	A_{σ_c}	$A_{c_{ii}}$	$\Delta x/\eta_{42d}$
0	0	100	0.107	0.37	(NA)	(NA)	2.8
1.1	0.8	240	0.150	0.51	(NA)	(NA)	2.3
2.1	1.6	259	0.021	0.10	5.10	3.50	1.5
3.2	2.4	263	0.019	0.11	4.90	3.30	1.0
4.3	3.2	248	0.026	0.12	4.40	2.85	0.8

Table 1. Physical and computational parameters of the DNS of viscoelastic turbulent planar wakes: global/inlet Weissenberg number ($Wi = \tau_p \Delta U_0/d$); polymer relaxation time (τ_p); Taylor-based Reynolds number at the far-field region (Re_λ); spreading rate constant A_δ ; centreline velocity deficit decay rate $A_{\Delta U}$; polymer stresses decay constant A_{σ_c} ; polymer extension decay constant $A_{c_{ii}}$; grid spacing normalised by the Kolmogorov microscale at the middle of the computational domain ($y/d = 0$ and $x/d = L_x/2d = 42$) ($\Delta x/\eta_{42d}$).

tensor field. The full version of the method requires the calculation of the eigenvalues of $54 \times N_x \times N_y \times N_z$ three by three matrices at each Runge–Kutta time iteration, a number of order $O(10^{10})$ for the computational meshes used in the present study. Unlike as in Guimarães *et al.* (2020), in the present work the computation of the eigenvalues has been abandoned in order to reduce the computational costs, so that the approximation used in the computation of the convection term of the conformation tensor equation was fixed into first order. This leads to a speed-up of a factor of four in the present code and allows one to use extremely large domain sizes. Despite the lower order of this approximation compared with Guimarães *et al.* (2020), the computational meshes used in the present study remain considerably fine, of the order of one Kolmogorov microscale for all the viscoelastic cases at large Wi ($\Delta x/\eta \approx 1$, see table 1) and thus the simplification has no impact on the conclusions of the work. This is shown in Appendix B, where one of the simulations used in the main text of the present work is repeated with the full second-order version of the method of Vaithianathan *et al.* (2006). Whereas the wake half-width and velocity deficit are virtually unchanged by the choice of the numerical method, the Reynolds stresses are slightly underestimated with the first-order method and the biggest ($i, j = 1, 1$) component of the conformation tensor shows the largest differences at the transition region of the flow, but follows the same qualitative trends everywhere else, i.e. in the fully developed turbulence region.

2.3. Physical and computational parameters of the simulations

Table 1 lists the physical and computational parameters used in the simulations carried out in this work (viscoelastic numbers are defined later on). A total of five DNS were performed: four viscoelastic cases and one reference Newtonian case. The same uniform grid and computational domain sizes were used for all DNS, with $N_x = 4032$, $N_y = 1152$ and $N_z = 288$ grid points in the streamwise (x), normal (y) and spanwise (z) directions, respectively, for a corresponding domain size of $L_x/d = 84$, $L_y/d = 24$ and $L_z/d = 6$, where d is the transverse length scale of the wake generator object. The results discussed in Appendix A confirm that the normal dimension of $L_y/d = 24$ used here is sufficiently large to avoid undesirable confinement effects. To date the present DNS correspond to the largest simulations of turbulent viscoelastic FENE-P fluids in existence.

The Reynolds number based on the centreline velocity deficit at the inlet ΔU_0 was fixed at $Re_{\Delta U} = \Delta U_0 d/\nu^{[s]} = 5000$, for all the simulations, which corresponds to a Reynolds

number based on the free stream velocity U_∞ ,

$$Re = \frac{U_\infty d}{\nu^{[s]}}, \quad (2.5)$$

approximately equal to $Re \approx 14\,286$, which is a definition more commonly used in studies of turbulent wakes originated at solid bodies. We define also a local Reynolds number based on the Taylor microscale λ ,

$$Re_\lambda = \frac{\sqrt{u'^2} \lambda}{\nu^{[s]}}, \quad (2.6)$$

where $\sqrt{u'^2}$ is the root mean square (r.m.s.) velocity in the streamwise direction and the Taylor microscale λ is calculated using the classical isotropic relation,

$$\lambda = \sqrt{\frac{15\nu^{[s]}u'^2}{\varepsilon^{[s]}}, \quad (2.7)$$

with the mean viscous dissipation rate of the solvent given by

$$\varepsilon^{[s]} = 2\nu^{[s]}\overline{S'_{ij}S'_{ij}}, \quad (2.8)$$

where $S'_{ij} = (\partial u'_i/\partial x_j + \partial u'_j/\partial x_i)/2$ is the fluctuating component of the rate-of-strain tensor. For the Newtonian (reference) simulation, the centreline Re_λ approaches a constant value of $Re_\lambda \approx 100$ at the far field, which is approximately two times larger than in a recent experimental study on the self-similar character of cylinder wakes (Tang *et al.* 2016). The mesh resolution is quantified by the ratio between the grid spacing Δx and the Kolmogorov microscale $\eta = (\nu^{[s]3}/\varepsilon^{[s]})^{1/4}$. The values of $\Delta x/\eta$ shown on table 1 were evaluated in the middle of the computational domain, i.e. at the centreline ($y/d = 0$) and at $x/d = L_x/2d = 42$.

For each time step the streamwise velocity $u(x, y, z, t)$ is prescribed at the inlet as the sum of a mean profile given by

$$\bar{u}(x = 0, y) = U_\infty - \frac{\Delta U_0}{2} \left\{ 1 + \tanh \left[\frac{d}{4\Phi} \left(1 - \frac{2|y|}{d} \right) \right] \right\}, \quad (2.9)$$

and a fluctuating component $u'(x, y, z, t)$, which is obtained from a pseudorandom number generator with the resulting fluctuating velocity exhibiting an energy spectrum $E(k)$ characteristic of isotropic turbulence, with an infrared region following a Batchelor spectrum, $E(k) \sim k^4$ (k is the wavenumber vector in the x, z inlet plane) and a prescribed peak wavenumber k_p placed at the small scales of motion. This is done so that no relation with the ‘natural’ Kelvin–Helmholtz frequencies of the shear layer exists (Michalke 1965; Monkewitz & Huerre 1982), which allows the momentum equations to ‘naturally select’ the natural instabilities of the flow. The initial inlet artificial noise is then ‘convoluted’ by a step function that prescribes it in the shear-layer region of the mean velocity profile (100 % of the generated fluctuations) and at the centre of the wake (25 % of the fluctuations). Before being imposed to the inlet velocity fluctuations, the instantaneous values of $u'(x, y, z, t)$ artificially generated are normalised to limit their maximum amplitude to $\max|u'| = 0.15U_\infty$. The entire procedure is very similar to the one described in detail in for example da Silva & Métais (2002), and has no influence in the natural evolution of

initial instabilities of the flow. The free stream velocity U_∞ and the inlet mean velocity deficit ΔU_0 were set to $U_\infty = 1$ and $\Delta U_0 = 0.35U_\infty$, respectively, where the latter is close to the value obtained in the experiments of Liu, Thomas & Nelson (2002). The parameter d/Φ in (2.9) dictates the value of the maximum mean velocity gradient at the inlet and it was fixed at $d/\Phi = 85$, giving $d\bar{u}/dy \sim 21.25\Delta U_0/d$ at the shear layer region of the profile. The normal and spanwise velocity components, $v(x, y, z, t)$ and $w(x, y, z, t)$, are treated similarly but have zero mean values, e.g. $v(x, y, z, t) = v'(x, y, z, t)$.

The inlet condition described above is similar to those used in Stanley & Sarkar (1997) and da Silva *et al.* (2015) for simulations of turbulent jets and mixing layers and Hickey, Hussain & Wu (2013) and Zecchetto & da Silva (2021) for simulations of temporal wakes, but was adapted to the case of a spatially evolving turbulent wake. This method for simulating turbulent wakes with an imposed inlet velocity profile, instead of actually calculating the flow around the solid object, was probably used for the first time by Moser, Rogers & Ewing (1998) and has been shown to be a useful technique for studying the far-field regions of the flow with an acceptable computational cost.

In the literature of Newtonian turbulent wakes, the distance x from the wake generator object is usually normalised either by the object transverse length scale d or by the inlet momentum thickness $\theta(x = 0)$, where θ is defined by

$$\theta = \int_{-\infty}^{\infty} \frac{\bar{u}}{U_\infty} \left(1 - \frac{\bar{u}}{U_\infty}\right) dy, \tag{2.10}$$

which is constant in the far field of a turbulent planar wake with a small velocity deficit. To simplify the notation, we use $\theta = \theta(x = 0)$ so when reference is made to θ only the inlet value is being considered. We have reprocessed the data for turbulent planar wakes of Newtonian fluids from several works (Pot 1979; Ramaprian 1984; Browne & Antonia 1986; Wygnanski, Champagne & Marasli 1986; Weygant & Mehta 1989; Aronson & Löfdahl 1993; Liu *et al.* 2002; Tang *et al.* 2016), as obtained behind solid objects with a variety of different geometries including splitter plates, circular cylinders, airfoils, solid strips and screens, and concluded that the scaling laws coefficients associated with the spreading rate of the wake A_δ and centreline velocity deficit decay rate $A_{\Delta U}$ (see (3.1) and (3.2) below) cannot be made universal by either normalisation options, i.e. using either d or θ . However, when d is used instead of θ , the scatter in the values of these constants is considerably larger. This is particularly true for $A_{\Delta U}$, which varies between $0.137 \leq A_{\Delta U} \leq 2.91$ when d is used as the normalisation parameter, and between $0.225 \leq A_{\Delta U} \leq 0.411$ when θ is used instead. For this reason, and following Wygnanski *et al.* (1986), we display our DNS results in coordinates of x/θ instead of x/d . The conversion between the two systems can be easily obtained for our data considering that the value of d/θ for all the simulations carried out in this work is $d/\theta = 4.34$, for example the total extent of the domain in the streamwise direction is equal to $L_x/\theta = L_x/d \times d/\theta = 84 \times 4.34 \approx 365$ in all the simulations carried out in the present work.

For rheological parameters of the FENE-P model we use $L^2 = 100^2$ and $\beta = \nu^{[s]}/(\nu^{[s]} + \nu^{[p]}) = 0.8$ in all the DNS carried out here, while τ_p is varied in order to simulate flows with different values of the global (or inlet) Weissenberg number Wi , which is defined by

$$Wi = \frac{\tau_p}{d/\Delta U_0}. \tag{2.11}$$

Notice that a definition of Wi based on the actual mean velocity gradient, instead of the velocity difference, would give values of Wi that are 21.25 times larger than those shown in table 1. We also define a local Weissenberg number $Wi_\eta(x)$ based on the ratio of the

maximum relaxation time of the polymer molecules and the Kolmogorov time scale $\tau_\eta = (\nu^{[s]}/\varepsilon^{[s]})^{1/2}$, which is computed at the centreline, i.e.

$$Wi_\eta(x) = \frac{\tau_p}{\tau_\eta}, \quad (2.12)$$

and a local Deborah number $De(x)$, which measures the influence of the fluid elasticity on the large scale energy-carrying eddies, here defined by

$$De(x) = \frac{\tau_p}{\delta(x)/\Delta U(x)}, \quad (2.13)$$

where $\delta(x)$ is the half-width of the wake, defined in the classical way, i.e. $\Delta\bar{u}(x, y = \delta) = \Delta U(x)/2$, where $\Delta\bar{u}(x, y) = U_\infty - \bar{u}(x, y)$ is the mean velocity deficit, while $\Delta U(x) = \Delta\bar{u}(x, y = 0)$ is the local velocity deficit at the centreline. Notice that (2.13) contains the centreline velocity deficit instead of the mean velocity (as in the case of jets, e.g. Guimarães *et al.* (2020)) because the Deborah number definition is based on a flow time scale obtained from the mean velocity gradient, whose estimate is given by $\partial\bar{u}/\partial y \sim \Delta U/\delta$. Also, notice that because the flow half-width at the inlet is $\delta(x = 0) \approx d/2$ we obtain $De(x = 0) \approx 2Wi$ at this location, as confirmed below in § 3.2.

Finally, as in Ferreira *et al.* (2016), we define a solvent dissipation reduction parameter (SDR) evaluated at the centreline of the turbulent viscoelastic wake by

$$SDR(x) = \frac{\varepsilon^{[p]}}{\varepsilon^{[p]} + \varepsilon^{[s]}}, \quad (2.14)$$

where $\varepsilon^{[p]} = \overline{\boldsymbol{\sigma}'^{[p]} : \nabla \mathbf{u}' / \rho}$ is the viscoelastic stress power and represents the flux of kinetic energy transported from the eddy motions into the fluid microstructure (and *vice versa*).

2.4. Validation

As described in Guimarães *et al.* (2020) and references therein, the present code has been used in several previous works where it has been thoroughly validated. In particular the work leading to that paper involved extensive validations in both laminar and turbulent jet configurations, using both Newtonian and viscoelastic (FENE-P) fluids. The solutions of the laminar cases were compared with the semianalytical solutions of the laminar viscoelastic jet recently derived by Parvar, da Silva & Pinho (2020), while the turbulent solutions were extensively compared with statistics obtained in experimental and numerical results available in the literature. A similar approach has been used here for the reference turbulent Newtonian planar wake. Part of the extensive comparison is described in Appendix A in which the present results are compared with the experimental and numerical data from Townsend (1949), Uberoi & Freymuth (1969), Narasimha & Prabhu (1972), Browne & Antonia (1986), Wignanski *et al.* (1986), Weygandt & Mehta (1989), Aronson & Löfdahl (1993), Zhou & Antonia (1995), Moser, Kim & Mansour (1999), Schenck & Jovanovic (2002), Hickey *et al.* (2013) and Tang *et al.* (2016). The influence of the lateral (L_y) size of the computational domain was also investigated (see Appendix A) and showed that no undesired confinement effects exist in the very large simulations used here.

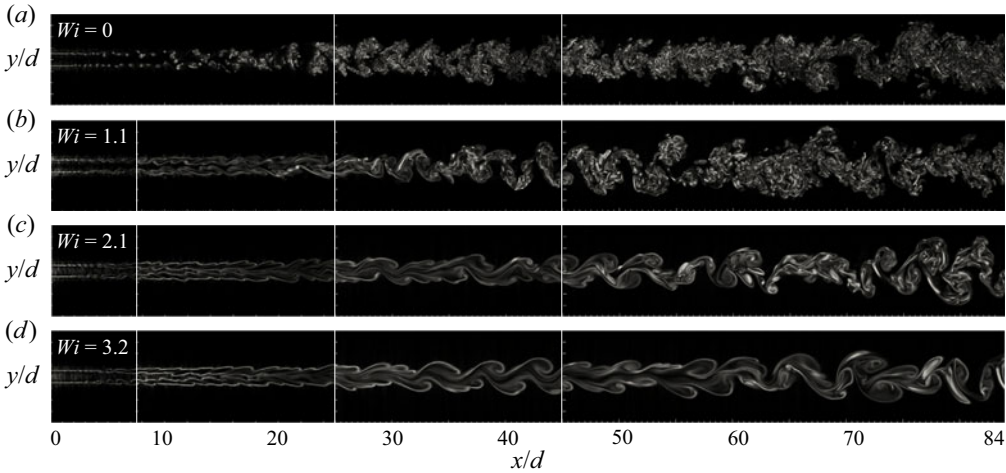


Figure 1. Contours of vorticity magnitude in the midplane ($z = 0$) of the computational domain for turbulent planar wakes of viscoelastic fluids with different values of the Weissenberg number $Wi = 1.1, 2.1$ and 3.2 , together with the reference (Newtonian) case ($Wi = 0$). Each simulation contains the entire domain (with $0 \leq L_x/d \leq 84$), however, different values of the vorticity magnitude threshold had to be used for each simulation in order to allow the visualisation of the flow in the entire computational domain (every subdomain using the same threshold is delimited by a vertical line). The figures do not show the total extent of the computational domain used in the lateral (y) dimension.

3. Characteristics of turbulent planar wakes of viscoelastic fluids

In this section we analyse the results obtained from the present DNS of turbulent viscoelastic planar wakes. We start the analysis describing the flow structure before moving into the turbulent wake statistics. In this process the Newtonian ($Wi = 0$) planar wake described in [table 1](#) is used as reference.

3.1. Contours of instantaneous vorticity magnitude

[Figure 1](#) shows contours of instantaneous vorticity magnitude $|\omega|$ for the DNS listed in [table 1](#) with Weissenberg numbers equal to $Wi = 1.1, 2.1$ and 3.2 , together with the reference (Newtonian) case ($Wi = 0$). Because the values of $|\omega|$ decay in the streamwise direction x , different colormap ranges were used at different regions of the computational domain in order to properly visualise the flow. Furthermore, since $|\omega|$ considerably decays when Wi is increased, the colormaps range is also different for the different Weissenberg number cases. For example, the maximum $|\omega|$ shown for the Newtonian case at the far field is $|\omega| = 10$, while we have set $|\omega| = 4$ for $Wi = 3.2$. The case with $Wi = 4.3$ is very similar to that with $Wi = 3.2$ (not shown).

For the Newtonian wake ($Wi = 0$ – [figure 1a](#)), Kelvin–Helmholtz instabilities arising in the upper and lower shear layers lead to the appearance of two rows of spanwise vortex rollers rotating in opposite directions – quasi-2-D Kármán vortices – and the formation of streamwise large vortex pairs due to the deformation of the primary vortices ($4 \lesssim x/d \lesssim 12$). Farther downstream, the flow structures are distorted by small-scale instabilities and by $x/d \gtrsim 25$ (or $x/\theta \gtrsim 100$) the flow becomes highly disorganised and with a broad range of eddy scales, characteristic of fully developed turbulence.

The results from the viscoelastic simulations are considerably different from the Newtonian case ([figure 1b–d](#)). Increasing the value of Wi has a stabilising effect on the

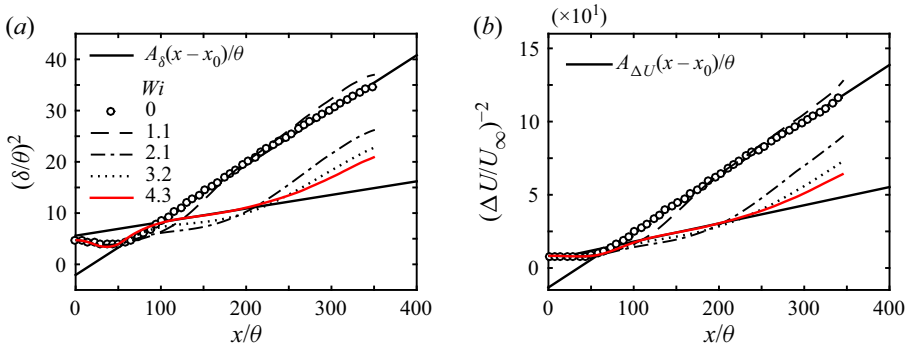


Figure 2. Streamwise evolution of the (a) squared shear layer thickness $\delta(x)^2$ normalised by the inlet momentum thickness θ and (b) centreline velocity defect $\Delta U(x)$ normalised by the free stream velocity U_∞ , for the DNS of viscoelastic turbulent planar wakes with Weissenberg numbers equal to $Wi = 1.1, 2.1, 3.2$ and 4.3 ($Wi = 0$ is the reference Newtonian simulation). The solid lines indicate straight line fits to the cases $Wi = 0$ (Newtonian) and $Wi = 4.3$.

flow structures; the roll-up process of the shear layers appears to be delayed and there is a significant suppression of the small-scale vorticity, consistent with results obtained from earlier experiments (Cadot & Kumar 2000; Cressman *et al.* 2001), numerical simulations (Richter *et al.* 2012) and linear stability analyses (Azaiez & Homsy 1994; Richter, Shaqfeh & Iaccarino 2011). In particular, the vortex sheet structure for $Wi = 2.1$ at $10 \lesssim x/d \lesssim 50$ (or $50 \lesssim x/\theta \lesssim 200$) is very similar to the structure observed in the soap film experiment of Xiong *et al.* (2013) with the highest polymer concentration, and for $x/d \gtrsim 60$ (or $x/\theta \gtrsim 250$) the roll-up of these vortex sheets leads to a structure which resembles the Newtonian case, but without much small-scale vorticity. Consistent with this, the next section shows that for $Wi = 2.1$ the statistical quantities mainly associated with the large-scale structures, such as the first and second moments of the velocity field, are greatly modified by the presence of the polymers at $10 \lesssim x/d \lesssim 50$ but seem to recover a Newtonian appearance at $x/d \gtrsim 60$.

3.2. Classical statistics

Figure 2(a,b) shows the streamwise evolution of the normalised shear layer thickness $\delta(x)$ and centreline velocity deficit $\Delta U(x)$ for the DNS of viscoelastic planar wakes with $Wi = 1.1, 2.1, 3.2$ and 4.3 . The reference Newtonian solution ($Wi = 0$) is also shown. In all cases the shear layer thickness follows a power law given by

$$\left[\frac{\delta(x)}{\theta} \right]^2 = A_\delta \left(\frac{x - x_0}{\theta} \right), \tag{3.1}$$

where A_δ is the spreading rate constant and x_0 is the virtual origin of the wakes. This is observed only after a given initial distance from the wake origin, which is approximately $x/\theta \gtrsim 60$ for the Newtonian wake, and which increases up to $x/\theta \gtrsim 100$ for the viscoelastic case with the larger Wi . It is well known that Newtonian turbulent planar wakes follow this power law, which is consistent with the existence of a fully developed self-similar regime (see the discussion below in § 4), however, this power law has rarely been observed in turbulent wakes of viscoelastic fluids. The value of the spreading rate A_δ for all the simulations is displayed on table 1. It is clear that for $Wi \geq 2.1$ the presence of the polymers substantially decreases the value of A_δ : we obtain $A_\delta = 0.107$

for the reference Newtonian turbulent wake, which is very close to the experimental value of $A_\delta = 0.102$ from Wygnanski *et al.* (1986) for the wake behind an airfoil, while A_δ is considerably smaller for $Wi \geq 2.1$, reaching a value as low as $A_\delta = 0.026$ for the viscoelastic case with the highest Weissenberg number, $Wi = 4.3$. The strong attenuation of the spreading rates of turbulent viscoelastic wakes is consistent with the decrease of the turbulent entrainment flow rate across the turbulent/non-turbulent interface recently investigated in Abreu *et al.* (2022).

Interestingly, the initially strong reduction of the spreading rate observed for the viscoelastic cases is, however, ‘temporary’ since very far from the inlet a Newtonian behaviour is recovered, i.e. in the far field of fully developed turbulent viscoelastic wakes with large Wi two different regions with power law $\delta(x) \sim x^{1/2}$ and different A_δ , can be identified. An initial region where the spreading rate constant A_δ is substantially reduced when compared with the reference Newtonian case, followed by a second region where the Newtonian spreading rate is recovered. Moreover, the Weissenberg number strongly influences not only the (reduced) value of A_δ in the initial region, as well as its spatial extent. This can be appreciated by comparing the cases with $Wi = 2.1$ and $Wi = 4.3$, where one can see that the extent of the (initial) region with a strong spreading rate reduction increases with the inlet Weissenberg number (see the discussion in Appendix C). While the simulation with $Wi = 2.1$ shows a clear reversal back into the Newtonian value of $A_\delta \approx 0.11$ at the far field, the computational domain used for $Wi = 4.3$ is still not long enough to reach a definite conclusion for that particular case. A straight line fit to $\delta^2(x)$ at $x/\theta \gtrsim 270$ gives $A_\delta = 0.08$, suggesting that a similar (Newtonian recovery) effect will be observed farther downstream. The case with $Wi = 1.1$ displays relatively small viscoelastic effects, however, it seems to display an incipient increased spreading rate region at $100 \lesssim x/\theta \lesssim 180$, but this region is quickly followed by a region (for $x/\theta \gtrsim 200$) where the spreading rate is equal to the Newtonian value $A_\delta \approx 0.1$. This situation is similar to that of viscoelastic turbulent jets for low Weissenberg numbers (Guimarães *et al.* 2020).

The streamwise evolution of the centreline velocity deficit, $\Delta U(x)$, is consistent with the results for $\delta(x)$ discussed above, and shows that in all cases (after a given distance x), again the usual scaling law observed for turbulent Newtonian planar wakes is observed, i.e.

$$\left[\frac{\Delta U(x)}{U_\infty} \right]^{-2} = A_{\Delta U} \left(\frac{x - x_0}{\theta} \right), \quad (3.2)$$

where $A_{\Delta U}$ is the velocity deficit decay rate, whose values are listed in table 1. For the Newtonian wake simulation we obtain $A_{\Delta U} = 0.374$, which is in very good agreement with the value of $A_{\Delta U} = 0.365$ measured by Weygandt & Mehta (1989) for a splitter plate, and with the values $A_{\Delta U} = 0.411$ and $A_{\Delta U} = 0.359$ obtained for an airfoil and a solid screen with 70% solidity, respectively, measured by Wygnanski *et al.* (1986). Consistent with the results discussed for $\delta(x)$, initially there is a drastic reduction of the velocity deficit decay rate when $Wi \geq 2.1$ ($A_{\Delta U} = 0.124$ for $Wi = 4.3$) but a Newtonian behaviour seems to be recovered very far from the wake generator object. As before, increasing the value of the inlet Weissenberg number Wi increases the extent of the initial region with strong viscoelastic effects and strong reduction of $A_{\Delta U}$. The case with $Wi = 1.1$ shows a small initial increase of $A_{\Delta U}$ but it later returns to the Newtonian value very far downstream, evidencing the existence of small viscoelastic effects for this case.

The decay of strong viscoelastic effects at the very far regions of viscoelastic wakes can be explained by analysing the streamwise evolution of the local Deborah number $De(x)$, which is shown in figure 3(a). The initially large values of $De(x)$ rapidly decay and at the end of the computational domain are approximately one order of magnitude

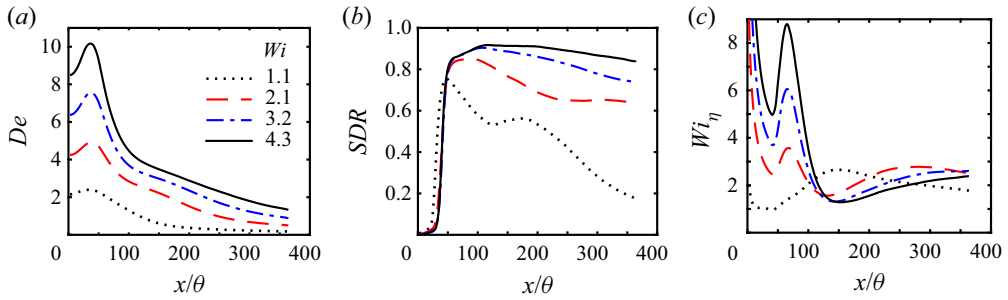


Figure 3. Streamwise evolution of the (a) local Deborah number $De(x) = \tau_p \Delta U / \delta$, (b) solvent dissipation reduction SDR and (c) local Weissenberg number $Wi_\eta = \tau_p / \tau_\eta$ (computed at the centreline) for all the viscoelastic wake simulations carried in the present work.

smaller than their maximum value (for each case). It is thus not surprising that statistical quantities characteristic of the large scales such as $\delta(x)$ and $\Delta U(x)$ will be less affected by the polymers at very large distances downstream.

Figure 3(b,c) shows the streamwise evolution of the solvent dissipation reduction $SDR(x)$ and local Weissenberg number Wi_η , respectively, both evaluated at the centreline of the wakes. The SDR initially increases and attains a maximum at $x/\theta \approx 50$ – 100 , depending on the value of the inlet Weissenberg number Wi , and starts to decay farther downstream with a decay rate which is smaller as the value of Wi is increased. The case with $Wi = 4.3$ shows $SDR > 0.8$ throughout all the computational domain, which implies that in this case the majority of the turbulent kinetic energy is dissipated by interactions between the polymers and velocity gradients, and not by molecular viscosity effects. Even the simulation with $Wi = 2.1$ shows an initially very high $SDR \approx 0.8$ at $50 \lesssim x/\theta \lesssim 100$ that decays to $SDR \approx 0.6$ for $x/\theta \gtrsim 200$. This important observation is used in the development of the theory exposed in § 4, which rests on the assumptions that for flows with large Wi , the viscous dissipation of turbulent kinetic energy plays only a minor role on the dynamics of the turbulent kinetic energy. A similar assumption was used in Guimarães *et al.* (2020) to develop the theory for viscoelastic turbulent planar jets.

Finally, it is noteworthy that for $Wi \geq 3.2$, the local Weissenberg number Wi_η is also considerably larger at $x/\theta \lesssim 90$ than farther downstream and for most of the simulations we have $Wi_\eta > 3$ at these initial regions. In particular, for $Wi = 3.2$ and $Wi = 4.3$ the maximum values of Wi_η are $Wi_\eta \approx 6$ and $Wi_\eta \approx 9$, respectively, which is already above the range of values of $Wi_\eta \sim 3$ – 5 where the coil-stretch transition occurs, as suggested by Watanabe & Gotoh (2010), and where a sharp increase in elongational viscosity is observed (Metzner & Metzner 1970; Tirtaatmadja & Sridhar 1993; Horiuti *et al.* 2013). However, even the cases with the larger inlet Weissenberg number have $Wi_\eta < 3$ for $x/\theta \gtrsim 150$, implying a strong decrease of the viscoelastic effects on the small-scale eddies of the distant far field. The only viscoelastic simulation where $Wi_\eta < 3$ throughout the whole computational domain is for $Wi = 1.1$, and therefore it is possible that for this case most of the polymer chains have not yet transitioned from the coiled to the stretched configuration. This explains the qualitatively different behaviour observed for this case compared with the cases with larger Wi described above. The coil-stretch transition explains also the non-monotonic behaviour of the integral quantities, $\delta(x)$ and $\Delta U(x)$ as Wi is increased. As discussed in the introduction, similar non-monotonic observations

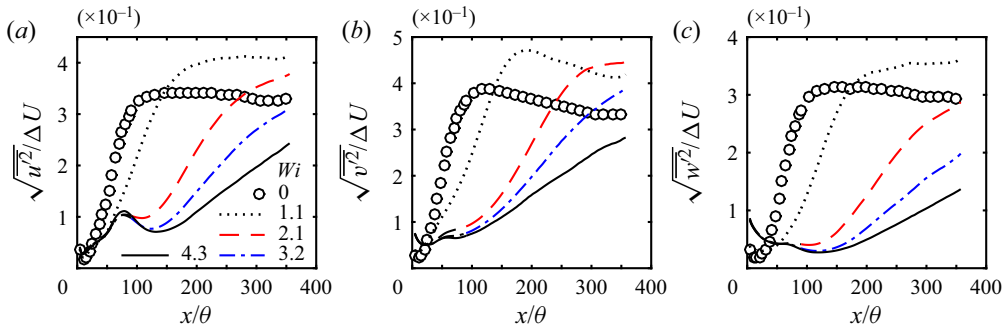


Figure 4. Streamwise evolution of the r.m.s. velocity components $\sqrt{u'^2}$, $\sqrt{v'^2}$ and $\sqrt{w'^2}$ normalised by the mean velocity deficit $\Delta U(x)$ (at the centreline) for the viscoelastic turbulent wakes with different Weissenberg numbers. The reference Newtonian case ($Wi = 0$) is also shown.

have been reported in the literature. The explanation is likely associated with the fact that in the case $Wi = 1.1$ the polymers have not undergone a coil-stretch transition, while for the case $Wi = 2.1$ they have likely transitioned. Comparing the integral quantities $\delta(x)$ and $\Delta U(x)$ for the cases $Wi = 2.2, 3.2$ and 4.3 , i.e. where the polymers have undergone a coil-stretch transition, shows that the results for these three cases display a monotonic behaviour, which is consistent with this explanation.

Figure 4(a–c) shows the downstream evolution of the r.m.s. of the velocity components $\sqrt{u'^2}$, $\sqrt{v'^2}$ and $\sqrt{w'^2}$, normalised by $\Delta U(x)$ and evaluated at the wake centreline, for the viscoelastic planar wakes with $Wi = 1.1, 2.1, 3.2$ and 4.3 , together with the reference Newtonian wake. For the Newtonian wake, all components reach an approximate plateau for $x/\theta \gtrsim 100$ which is consistent with a fully turbulent self-similar regime. The viscoelastic simulations show an attenuation of the turbulent intensities as the value of the inlet Weissenberg number is increased, especially at regions where $De(x)$ is large, but show also a tendency for approaching the Newtonian values farther downstream. This is particularly evident for the cases with $Wi < 3.2$. In fact, for $Wi = 1.1$, the initially weaker r.m.s. velocities are slightly higher for $x/\theta \gtrsim 150$ than those of the Newtonian simulation. The data suggests a similar trend for larger values of Wi , but as Wi is increased the extent of the initial region with strong viscoelastic effects also increases, consistent with the discussion above related to $\delta(x)$ and $\Delta U(x)$.

To complement the description of the turbulent classical statistics, figure 5 shows transverse (y) profiles of mean velocity deficit and streamwise (normal) Reynolds stresses at two different stations. The two stations, $x/\theta = 200$ and $x/\theta = 315$, approximately correspond to the two locations where the scaling laws $\delta(x) \sim x^{1/2}$ and $\Delta U(x) \sim x^{-1/2}$ are observed for the cases with $Wi \geq 2.1$: (i) the region where we observe strong reductions in A_δ and $A_{\Delta U}$ ($x/\theta = 200$); and (ii) near the end of the computational domain ($x/\theta = 315$) where those two slopes are similar to the Newtonian slopes. In agreement with the experimental study of Borisov *et al.* (1990) the normalised mean velocity deficit $\Delta \bar{u}/\Delta U$ is not substantially changed by the presence of the polymers (figure 5a,b). In contrast, and consistent with the decrease in A_δ discussed before all components of the Reynolds stress tensor are substantially reduced at $x/\theta = 200$ as Wi is increased (figure 5c) (only one component is shown here for brevity). The drastic reduction of the values of the normalised Reynolds stresses, in particular for the cases with large Wi , is in qualitative agreement with the experimental results of Pokryvailo *et al.* (1973), Borisov *et al.* (1990),

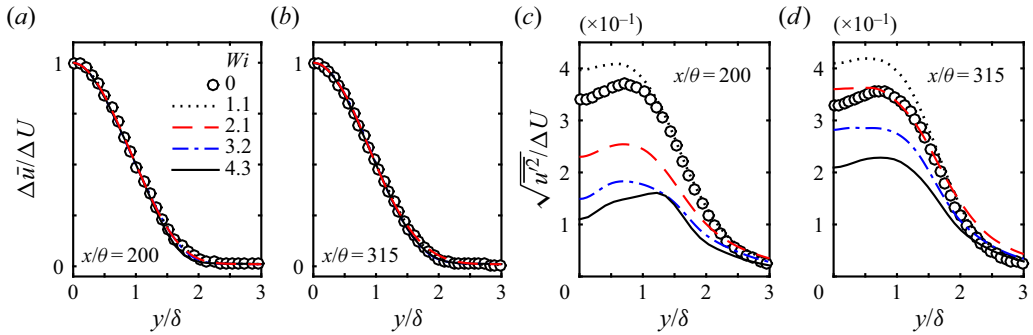


Figure 5. Transverse profiles of (a,b) mean (streamwise) velocity deficit $\Delta \bar{u}$ and (c,d) streamwise Reynolds stresses $\sqrt{w^2}$ at (a,c) $x/\theta = 200$ and (b,d) $x/\theta = 315$ for the simulations with $Wi = 0$ (Newtonian), $Wi = 1.1, 2.1, 3.2$ and 4.3 , normalised with the velocity defect $\Delta U(x)$ and the half-width $\delta(x)$.

Pinho & Whitelaw (1991) and Cressman *et al.* (2001). These earlier experimental studies were limited to the near field region of the wake ($x/d \leq 20$), while in the present study we attain $x/d \leq 84$, which possibly explains why none of them observed the return to an (approximately) Newtonian behaviour very far downstream of the wake generating object reported here (in the case of Pinho & Whitelaw (1991), the experiment involved a disk inside a pipe so that only the near wake region could be studied). This is again confirmed by the Reynolds stresses from the viscoelastic simulations at $x/\theta = 315$ (figure 5d) which become much closer to the Newtonian profiles. In fact, the lower Wi case shows a slight increase of the Reynolds stresses in comparison with the Newtonian case.

The results discussed above for the normal Reynolds stress components show that viscoelasticity has the analogous effect for all three components simultaneously. This is different from other flow configurations, for example flows in the proximity of solid walls at the low drag reduction regime, where the streamwise velocity component increases with Wi , while the other two components decrease, and only at the high drag reduction regime do all velocity components decrease together, as Wi increases (White & Mungal 2008). To explain the behaviour of the turbulent velocity fluctuations in more detail we consider the turbulent kinetic energy budgets, $\kappa = \overline{\mathbf{u}' \cdot \mathbf{u}'}/2$.

For this statistically stationary flow the balance equation for κ is given by

$$\begin{aligned} \bar{\mathbf{u}} \cdot \nabla \kappa = & -\frac{1}{\rho} \nabla \cdot \overline{p' \mathbf{u}'} - \frac{1}{2} \nabla \cdot \overline{\mathbf{u}' \mathbf{u}' \cdot \mathbf{u}'} + \nu^{[s]} \nabla^2 \kappa - \overline{\mathbf{u}' \mathbf{u}'} : \nabla \bar{\mathbf{u}} - \nu^{[s]} \overline{\nabla \mathbf{u}' : \nabla \mathbf{u}'} \\ & + \frac{1}{\rho} \nabla \cdot \overline{\boldsymbol{\sigma}'^{[p]} \cdot \mathbf{u}'} - \frac{1}{\rho} \overline{\boldsymbol{\sigma}'^{[p]} : \nabla \mathbf{u}'}. \end{aligned} \quad (3.3)$$

The last two terms in (3.3) are absent in Newtonian fluids and represent the viscoelastic turbulent transport and the viscoelastic stress power, respectively. The transverse profiles of all the terms from this equation, at a fixed station x/θ , are shown in figure 6. Comparing the Newtonian case with the viscoelastic case at low $De(x)$ (figure 6a with 6b) it can be seen that the viscoelastic fluid has a larger gain of turbulent kinetic energy from the advection term $\bar{\mathbf{u}} \cdot \nabla \kappa$, especially at the flow centreline $y/\delta(x) = 0$, but part of this energy is not dissipated by the solvent and is transferred to the polymer microstructure through the viscoelastic stress power term $\overline{\boldsymbol{\sigma}'^{[p]} : \nabla \mathbf{u}'}/\rho$, thus leading to slightly higher values of turbulent velocity fluctuations for that case. Other terms of the equation do not change significantly. However, for the high Deborah number case (figure 6c) we observe a large

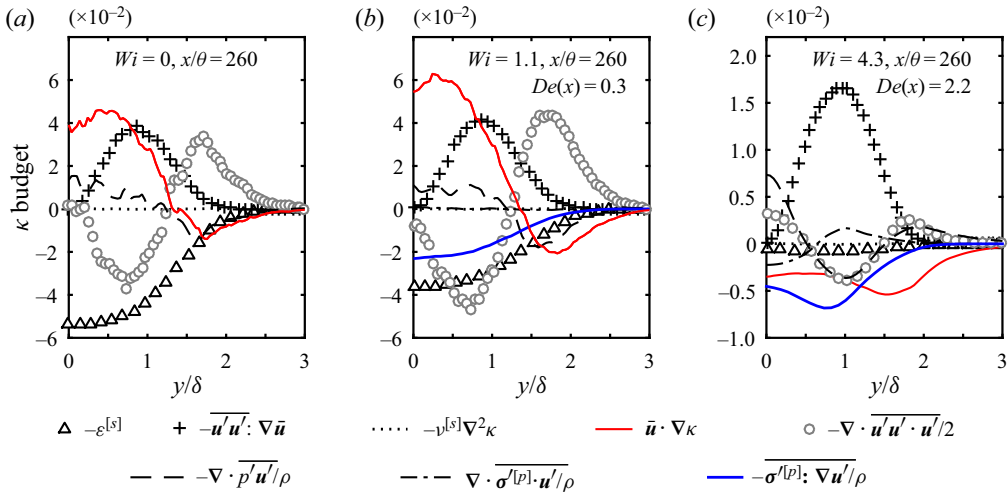


Figure 6. Budgets of turbulent kinetic energy (3.3) for (a) the Newtonian wake, (b) a viscoelastic wake at low Deborah number and (c) a viscoelastic wake at high Deborah number. In these figures all the terms in (3.3) have been normalised by $\Delta U(x)^3/\delta(x)$.

depletion of all terms of the equation, including the production term $-\overline{u'u'} : \nabla \bar{u}$, which results in the much lower levels of turbulent velocity fluctuations discussed above for high $De(x)$. Two additional observations for the high $De(x)$ case are (i) the advection term becomes a sink of turbulent energy in all the turbulent core region of the flow; and (ii) the dissipation of κ is done almost entirely by the polymers, since the solvent dissipation becomes negligibly small in comparison with the viscoelastic stress power.

The streamwise evolution of the viscous dissipation rate of the solvent $\varepsilon^{[s]}$ (computed at the centreline) is shown in figure 7(a) for different values of Wi and allows one to see in even more detail how the viscoelastic cases relate to the Newtonian reference simulation. While for the Newtonian case $\varepsilon^{[s]}$ attains a local maximum and starts to decay for $x/\theta \gtrsim 100$, for the viscoelastic cases (with $Wi \geq 2.1$) the corresponding local maxima are located slightly earlier and are much smaller (by one order of magnitude) than in the Newtonian case. Interestingly, after the local maximum is attained $\varepsilon^{[s]}$ reaches a local minimum and starts to increase towards the Newtonian value at the very far regions of the wake. The position of the local minimum moves downstream as the inlet Weissenberg number is increased and is located roughly at the centre of the region with reduced spreading and decaying rates described above. At these locations $\varepsilon^{[s]}$ for the viscoelastic cases with $Wi \geq 3.2$ is reduced by two orders of magnitude in comparison with the Newtonian flow. The reduction in $\varepsilon^{[s]}$ caused by the viscoelastic effects is therefore quite impressive. The shape of the curve for $Wi = 1.1$ is much different from the other viscoelastic cases, since it is similar to the Newtonian case but with a delayed position of the local maximum. There is also a strong reduction of $\varepsilon^{[s]}$ for $Wi = 1.1$ compared with the Newtonian case, but at the end of the computational domain we have a complete return to the Newtonian values. The results strongly suggest that the same trend would also be observed for the other simulations had the computational domain been longer in those cases.

The behaviour of $\varepsilon^{[s]}$ is strongly related to the behaviour of Wi_η , since from the definition of Wi_η we have $Wi_\eta = \tau_p/\tau_\eta = \tau_p \sqrt{\varepsilon^{[s]}/\nu^{[s]}}$, and naturally figures 7(a) and 3(c) are similar. The sudden peaks observed for $\varepsilon^{[s]}\theta/U_\infty$ (and for Wi_η) in the near field region ($x/\theta \lesssim 100$) seem to be connected with the coil-stretch transition, as if a sudden

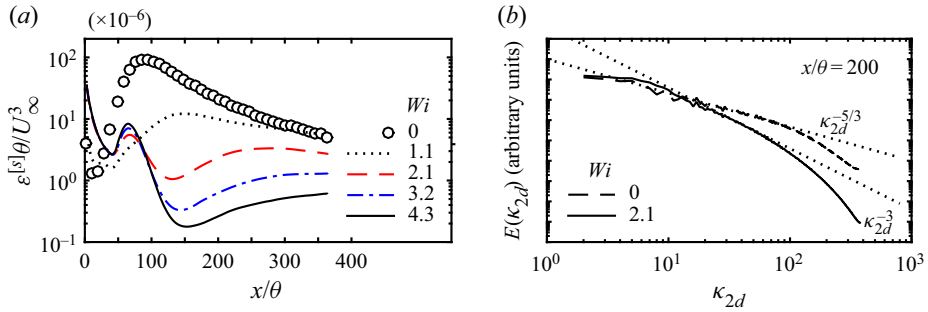


Figure 7. (a) Streamwise evolution of the normalised centreline viscous dissipation rate of the solvent and (b) 2-D kinetic spectrum of turbulent kinetic energy $E(k_{2d})$ at a fixed station $x/\theta = 200$ for different Weissenberg numbers.

increase of small-scale activity associated with an initial increase in the solvent dissipation triggers the coil-stretch transition, and results in the polymers strongly attenuating the local nonlinearity within the solvent and thus the solvent dissipation.

Finally, the dramatic reduction of $\varepsilon^{[s]}$ observed at regions with large values of the local Deborah number $De(x)$ is a result of the different energy cascade mechanism that is known to exist for viscoelastic turbulence (Valente, da Silva & Pinho 2014, 2016). This results in spectra with an inertial-elastic region with $E(k) \sim k^{-3}$, instead of the typical $E(k) \sim k^{-5/3}$ of classical (Newtonian) turbulence. The present DNS also recover these two cases as can be attested in figure 7(b) showing the 2-D kinetic energy spectra $E(k_{2d})$ obtained at $x/\theta = 200$, for the Newtonian and $Wi = 2.1$ cases, where $k_{2d} = (k_2^2 + k_3^2)^{1/2}$ and k_2 and k_3 are the wavenumbers in the normal and spanwise directions, respectively. The spectrum is computed in the 2-D directions of the plane normal to the streamwise direction (y, z) using the usual procedure to compute a 2-D spectrum, as if the flow were homogeneous in these two directions. Although this is not the case and the resulting spectrum will not be physically realistic in the smallest wavenumbers, associated with the larger scale flow features, it will still be representative of the intermediate and small scales of motion, which are the ones that interest us in this figure. As can be seen, while the Newtonian spectrum follows the classical $-5/3$ power law at the inertial subrange, a -3 power law can be identified for the viscoelastic simulation, which is the same power law obtained in experiments of turbulence generated by a grid with polyethylene oxide solutions (Vonlanthen & Monkewitz 2013), viscoelastic jets (Yamani *et al.* 2021) and in simulations of forced homogeneous isotropic turbulence with the FENE-P model (Valente *et al.* 2014, 2016).

To complete the characterisation of the new DNS of turbulent viscoelastic wakes, and to give further insight into the interplay between the dynamics of the polymer chains and the turbulent flow, figure 8 shows streamwise profiles of the mean diagonal components of the conformation tensor (see also Appendix B where a comparison between two cases that use first- or second-order discretisation for the $\mathbf{u} \cdot \nabla \mathbf{C}$ advection term show some quantitative differences for the $\overline{C_{ij}}$ components at the transition region, especially for $\overline{C_{11}}$, but the same physical trends are obtained everywhere else, regardless of the order of the numerical method employed). As expected, the values of all C components increase with Wi at a given particular location and, for $Wi \geq 2.1$ the normal component on the principal (x) direction of the flow $\overline{C_{11}}$ is initially much larger than the other components, indicating that on average the polymer chains are considerably more stretched in that direction. This is also observed in the transverse (y) profiles of \overline{C} (not shown). However, for $x/\theta \gtrsim 100$

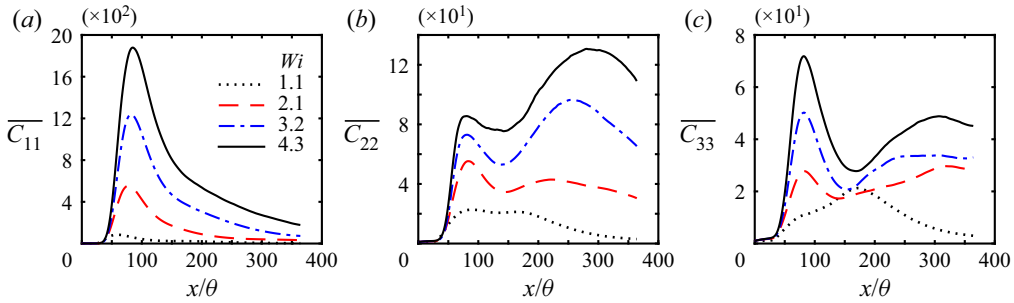


Figure 8. Streamwise evolution of the (mean) diagonal terms of the conformation tensor (computed in the centreline) for the present DNS of viscoelastic turbulent wakes.

the component \overline{C}_{11} decays faster than the other components and very far downstream there is a tendency for approaching a state where $\overline{C}_{11} \approx \overline{C}_{22} \approx \overline{C}_{33} \gg \overline{C}_{12}$, which is similar to the behaviour observed in a turbulent jet (Guimarães *et al.* 2020). The transverse profiles showed also that at regions where $De(x)$ is small and $\overline{C}_{11} \approx \overline{C}_{22} \approx \overline{C}_{33} \gg \overline{C}_{12}$ the maximum values of the \overline{C} components are located at the centreline of the wake $y/\delta = 0$, although the mean velocity gradient $\partial\overline{u}/\partial y$ is zero at these locations. This can be explained as follows: for small values of $De(x)$ the large turbulent eddies are poorly oriented with polymer molecules and the polymer stretch is predominately imposed by the small-scale eddies, which tend to be nearly isotropic, i.e. without a preferential direction, which explains why \overline{C} is approximately isotropic when $De(x)$ is small. When $De(x)$ is large, however, the strain rate is imposed by the anisotropic large scale eddies and has a bigger influence on the polymer elongation and on the maximum values of the \overline{C} components, which attain a maximum at $y/\delta \approx 0.8$, where $\partial\overline{u}/\partial y$ attains its peak.

4. The theory of viscoelastic turbulent planar wakes

This section proposes a (new) theory for the description of turbulent planar wakes with viscoelastic solutions, valid at the far-field region of the flow. The theory is based on the classical analysis of Newtonian turbulent wakes and uses the thin shear layer approximation applied to the equations for the transport of mass, momentum and turbulent kinetic energy, properly modified to take into account the polymeric additives. The scaling law for the polymer shear stress is based on the ideas put forward by Guimarães *et al.* (2020) and also adopts the time criterion of Lumley (1973) and Seyer & Metzner (1969), while no use of the FENE-P rheological model is made in the derivations. Finally, the theory allows the computation of the averaged polymer chain extension by using a simple viscoelastic fluid model to relate the polymer stresses and the conformation state of the polymeric chains.

4.1. Thin shear layer approximation

Under the thin shear layer approximation the mean momentum equation in the streamwise (x) direction can be written as

$$\overline{u} \frac{\partial \Delta \overline{u}}{\partial x} + \overline{v} \frac{\partial \Delta \overline{u}}{\partial y} = \frac{\partial \overline{u'v'}}{\partial y} - \frac{1}{\rho} \frac{\partial \overline{\sigma_{xy}^{[p]}}}{\partial y}, \tag{4.1}$$

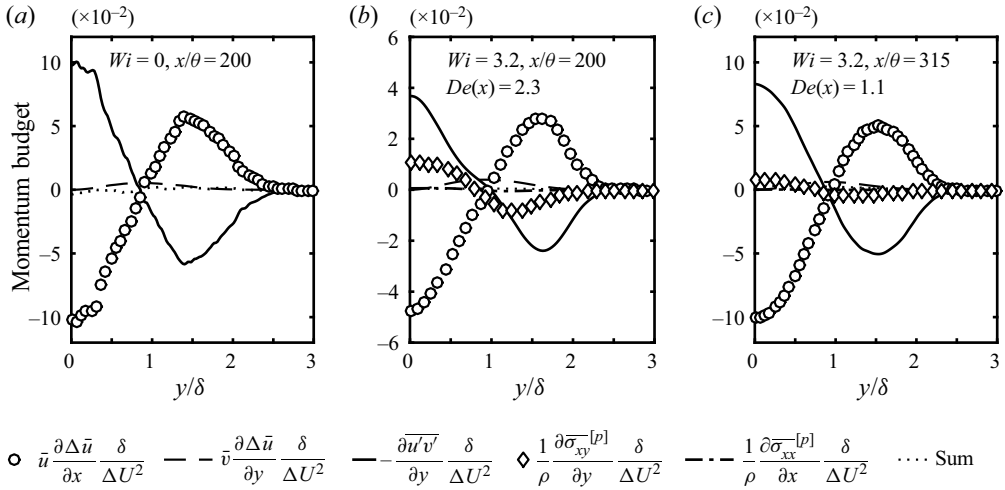


Figure 9. Transverse profiles of the terms from the mean streamwise momentum equation, with the thin shear layer approximation (4.1), for the reference Newtonian simulation at $x/\theta = 200$ (a), and for the viscoelastic simulation with $Wi = 3.2$ at $x/\theta = 200$ (b) and $x/\theta = 315$ (c). The terms are normalised by the velocity deficit $\Delta U(x)$ and by the thickness of the shear layer $\delta(x)$, and the dotted lines represent the sum of all the terms shown in the figures excluding the term $\rho^{-1} \partial \sigma_{xx}^{[p]} / \partial x$, which is neglected in the thin shear layer approximation.

where again $\Delta \bar{u}(x, y) = U_\infty - \bar{u}(x, y)$ is the mean velocity deficit, $\overline{u'v'}$ is the turbulent shear stress, and $\overline{\sigma_{xy}^{[p]}}$ is the mean polymer shear stress, while the mean continuity equation is

$$\frac{\partial \bar{u}}{\partial x} + \frac{\partial \bar{v}}{\partial y} = 0. \tag{4.2}$$

In (4.1) and (4.2) the classical assumptions of (i) high Reynolds number (viscous stresses can be neglected) and (ii) negligible gradients in the streamwise (x) direction compared with the normal (y) direction ($\partial/\partial y \gg \partial/\partial x$) have both been used. The momentum equation in the normal direction is treated in a similar way leading one to conclude that the mean pressure is constant in the flow domain, thus eliminating the mean pressure gradient term ($\partial \bar{p} / \partial x = 0$) originally in (4.1).

In order to assess the robustness of this (thin-shear layer) approximation in the present turbulent viscoelastic free flow configuration figure 9 shows all the terms from (4.1), for the Newtonian simulation at $x/\theta = 200$ (figure 9a) and for the viscoelastic simulation with $Wi = 3.2$ at two different locations, $x/\theta = 200$ (figure 9b) and $x/\theta = 315$ (figure 9c). Additionally, the term neglected in the approximation, $\rho^{-1} \partial \overline{\sigma_{xx}^{[p]}} / \partial x$ (streamwise gradient of the first normal polymer stress), and the sum of all the terms in the equation (denoted by ‘sum’) are also shown for comparison. It is clear that the thin shear layer approximation is very accurate in the present case. Inertia is balanced by the gradient of total (polymer plus turbulent) shear stress and the ‘sum’ is close to zero. The influence of viscoelasticity on the budget of momentum is also apparent from the figures. At $x/\theta = 200$, transport of momentum by turbulent velocity fluctuations is decreased in comparison with the Newtonian case by a factor larger than two and the gradient of polymer shear stress is an important term in the equation. However, at $x/\theta = 315$, where the local Deborah number $De(x)$ has decayed considerably, the budgets for the viscoelastic and Newtonian cases are very similar, the normalised Reynolds shear stress term has increased to the Newtonian values and the polymer stress term is very small in comparison with the other terms in

the equation. This is in agreement with the observations made on § 3 that describe the decay of the viscoelastic effects as the wake evolves downstream, and shows also that the polymer stresses decay faster than the turbulent stresses.

4.2. Self-similarity analysis

Rewriting (4.1) in conservative form and integrating in the transverse (y) direction yields

$$\frac{d}{dx} \int_{-\infty}^{\infty} \bar{u}(x, y) \Delta \bar{u}(x, y) dy = 0, \tag{4.3}$$

where boundary conditions of zero velocity deficit and zero turbulent and polymer shear stresses far from the wake centreline have been applied, i.e. $\Delta \bar{u}(x, y \rightarrow \pm\infty) = 0$, $\overline{u'v'}(x, y \rightarrow \pm\infty) = 0$ and $\overline{\sigma_{xy}^{[p]}}(x, y \rightarrow \pm\infty) = 0$, respectively. We now introduce the normalised velocity deficit,

$$\psi = \frac{\Delta \bar{u}(x, y)}{\Delta U(x)} \tag{4.4}$$

and the similarity coordinate,

$$\xi = \frac{y}{\delta(x)}. \tag{4.5}$$

The hypothesis of self-similarity of the mean velocity deficit implies that the function ψ only depends on the similarity coordinate ξ , and does not vary with the streamwise distance x , i.e. $\psi = \psi(\xi)$. Inserting the hypothesis of self-similarity in (4.3) leads to

$$\frac{d}{dx} [\Delta U(x) \delta(x)] = 0, \tag{4.6}$$

where the term of order $\Delta U^2(x)$ has been neglected, an approximation that becomes asymptotically exact in wakes in the limit of small velocity deficits.

Up to this point, the analysis is very similar to the classical theory of (Newtonian) wakes, and (4.6) is the usual momentum integral constraint. The classical theory derivation would continue by assuming self-similarity of $\overline{u'v'}$ when scaled by $\Delta U(x)^2$ (Townsend 1976). However, for the viscoelastic wake this assumption is not valid because the presence of the elasticity introduces an extra time scale that breaks the similarity of the profiles of $\overline{u'v'}/\Delta U(x)^2$ (this matter is discussed in detail on § 4.4), which is also observed in a viscoelastic turbulent jet (Guimarães *et al.* 2020). Here we take a different strategy and consider the equation for the mass conservation (4.2), which after a first integration and further algebraic manipulations can be rewritten in the following form:

$$\phi = \frac{-U_{\infty} \bar{v}(x, y)}{\Delta U^2(x)} = \frac{d\delta^2(x)}{dx} \left[\frac{U_{\infty}/2}{\Delta U(x)\delta(x)} \right] \{ \xi \psi(\xi) \}. \tag{4.7}$$

The quantity $-U_{\infty} \bar{v}(x, y)$ is the entrained momentum flux (by the normal velocity \bar{v}) from the free stream into the turbulent core of the wake, and ϕ is this momentum flux normalised by $\Delta U^2(x)$. It results from the momentum integral constraint (4.6) that the term inside square brackets in (4.7) is constant. Furthermore, the term inside curly brackets is a function of ξ only, and does not vary with x . The conclusion is that the assumption of self-similarity $\phi = \phi(\xi)$ can only be satisfied for all values of ξ if the spreading rate

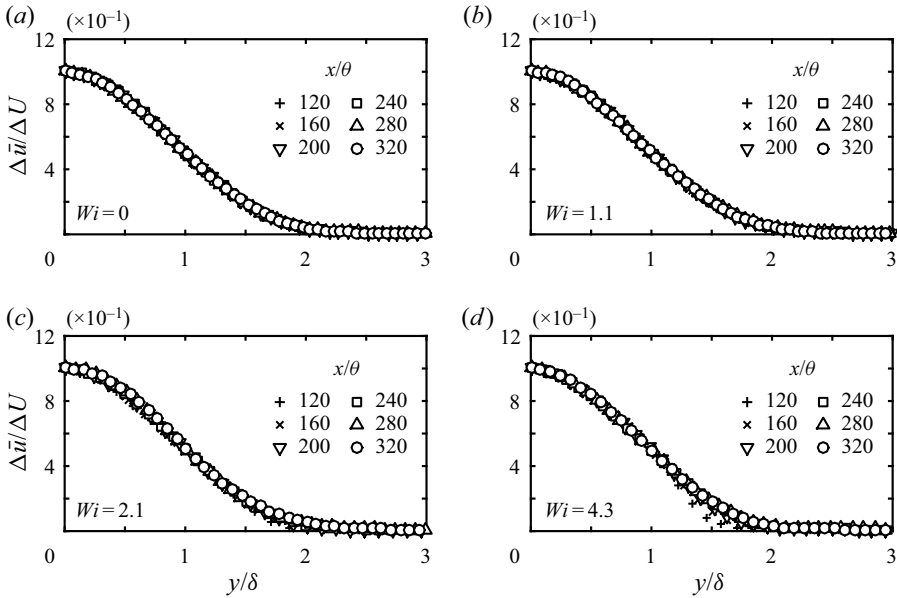


Figure 10. Transverse profiles of normalised mean velocity deficit at several stations x/θ for the Newtonian ($Wi = 0$) and viscoelastic simulations with Weissenberg numbers $Wi = 1.1, 2.1$ and 4.3 .

parameter $d\delta^2/dx$ reaches a constant value at the far field, which gives the following scaling law for the evolution of the half-width of the wake,

$$\delta(x) \sim x^{1/2}. \tag{4.8}$$

Substitution of (4.8) into (4.6) gives the scaling law for the velocity deficit,

$$\Delta U(x) \sim x^{-1/2}. \tag{4.9}$$

These scaling laws are, of course, the same laws obtained for the evolution of turbulent planar wakes with Newtonian fluids (Schlichting 1930), and have been observed here when discussing figure 2 in § 3. However, the coefficients in these scaling laws are very different for Newtonian and viscoelastic wakes, especially when the Deborah number is large, as demonstrated before in § 3 (see the values of A_δ and $A_{\Delta U}$ in table 1).

Figure 10 shows profiles of $\psi = \Delta\bar{u}(x, y)/\Delta U(x)$ from Newtonian and viscoelastic simulations at several x/θ stations. The excellent collapse of all the profiles validates the hypothesis of self-similarity of the mean velocity deficit. This is no surprise for the Newtonian case, while for viscoelastic cases it agrees with the experimental study of Borisov *et al.* (1990). The slightly less good collapse in the first profile for the case $Wi = 4.3$ (close to the wake edge) merely indicates that self-similarity is attained later for that case, as described before in § 3.2 when the evolutions of $\delta(x)$ and $\Delta U(x)$ were analysed. The case with $Wi = 3.2$ is virtually equal to that with $Wi = 4.3$, and is not shown in the figure for reasons of space.

Transverse profiles of $\phi = -U_\infty \bar{v}(x, y)/\Delta U^2(x)$ at several stations are shown in figure 11 for the Newtonian ($Wi = 0$) and the viscoelastic cases with Weissenberg numbers equal to $Wi = 1.1, 2.1$ and 4.3 . For the Newtonian case all the profiles collapse into one single curve when $x/\theta \gtrsim 150$. The viscoelastic case with $Wi = 1.1$ shows a similar collapse of the profiles for $x/\theta \gtrsim 210$, while the profiles at $x/\theta = 150$ and 180 are shifted

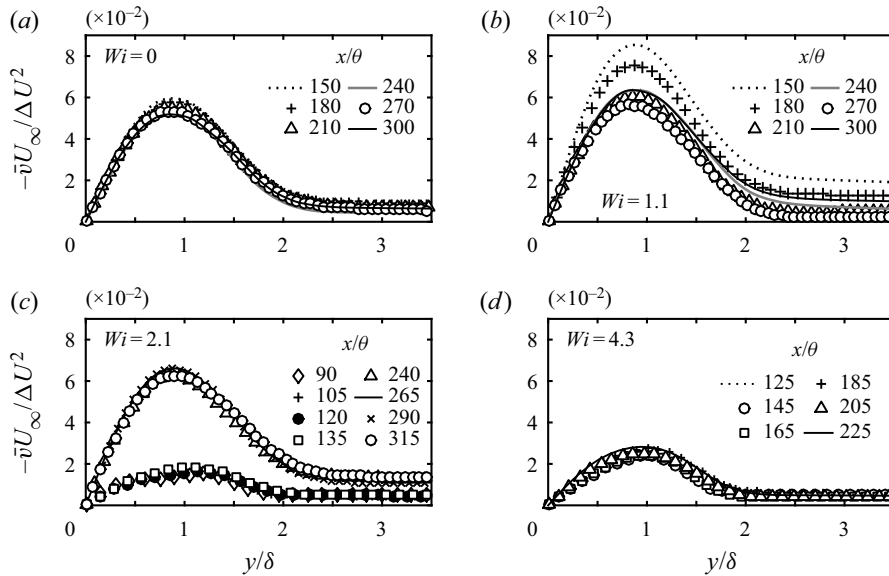


Figure 11. Transverse profiles of normalised normal mean velocity $\bar{v}(x, y)$ at several stations x/θ for the Newtonian ($Wi = 0$) and viscoelastic simulations with Weissenberg numbers $Wi = 1.1, 2.1$ and 4.3 .

upwards due the increased spreading rate observed for that case. For the viscoelastic case with $Wi = 2.1$, two different similarity curves can be identified. The profiles within the region $90 \lesssim x/\theta \lesssim 135$ collapse into a curve which has a maximum value of $\phi \approx 0.02$ while the profiles at $240 \lesssim x/\theta \lesssim 315$ collapse into a different curve that has a maximum of $\phi \approx 0.062$ and is much closer to the Newtonian curve. According to (4.7), this means that the spreading rate parameter $d\delta^2/dx$ assumes constant values in these two different regions, although with a much lower value at $90 \lesssim x/\theta \lesssim 135$ than at $240 \lesssim x/\theta \lesssim 315$. This is precisely what was observed for this case in § 3 when the streamwise evolution of δ^2 was analysed. At intermediate locations between these two regions of the flow, i.e. at $135 \lesssim x/\theta \lesssim 240$, the corresponding profiles of ϕ do not collapse (not shown for clarity) and $d\delta^2/dx$ is not constant, as it can be seen from figure 2 discussed before. For $Wi = 4.3$ we observe similarity of the profiles at $125 \lesssim x/\theta \lesssim 225$, which is the region where $d\delta^2/dx$ was found to be constant when figure 2 was analysed. The similarity curve for $Wi = 4.3$ has a maximum of $\phi \approx 0.028$, consistent with a much smaller spreading rate compared with the Newtonian case. The extent of the first similarity region with a strong decrease of the spreading rate is clearly longer when Wi is increased (approximately 100θ for $Wi = 4.3$ compared with 45θ for $Wi = 2.1$). We were unable to find a second similarity curve for $Wi = 4.3$ in the present simulations, but the discussion in § 3.2 strongly suggests that with a longer computational domain we would be able to observe the ϕ profile approaching the Newtonian curve at the distant far-field region for that case too.

The derivation outlined above in (4.3)–(4.7) is also interesting for the simpler case of a Newtonian wake, because it shows that the scaling laws $\delta(x) \sim x^{1/2}$ and $\Delta U(x) \sim x^{-1/2}$ can be obtained without making any assumption regarding the turbulent shear stress $\overline{u'v'}$, whose scaling has been subject to some controversy over the last years (George 2008). New theories of free turbulent flows often make assumptions about several other quantities, including the normal turbulent stresses and the viscous dissipation rate of turbulent kinetic

energy. The derivation discussed above clarifies that in fact, self-similarity of the mean velocities alone is sufficient to derive the classical scaling laws in the form of (4.8) and (4.9).

4.3. Similarity laws for the polymer shear stress and averaged polymer chain elongation

Guimarães *et al.* (2020) showed that in turbulent viscoelastic planar jets the profiles of mean polymer shear stress $\overline{\sigma_{xy}^{[p]}}(x, y)$ are self-similar when properly normalised. A similar result holds also in the present configuration of viscoelastic planar wakes as we now describe.

We proceed in a similar fashion by deriving an expression for the characteristic scale of the polymer shear stress $\sigma_c^{[p]}(x) = \max|\overline{\sigma_{xy}^{[p]}}(x, y)|$, which can be obtained from the transport equation for the turbulent kinetic energy $\kappa = \overline{\mathbf{u}' \cdot \mathbf{u}'}/2$, which for a steady mean flow is given by (3.3) discussed before. The explicit influence of viscoelasticity appears in the last two terms of this equation, which are the viscoelastic turbulent transport $\nabla \cdot \overline{\sigma'^{[p]} \cdot \mathbf{u}'}/\rho$ and the viscoelastic stress power $\overline{\sigma'^{[p]} : \nabla \mathbf{u}'}/\rho$. For wakes with sufficiently large Deborah numbers it is likely that at least one of these two terms will dominate, and will then need to be balanced by the remaining leading-order terms of the equation. An order of magnitude analysis of (3.3) shows that this leading-order term is the production term, which for the planar wake is of order (as shown further below)

$$-\overline{\mathbf{u}' \mathbf{u}'} : \nabla \bar{\mathbf{u}} \sim \frac{U_\infty \Delta U^2}{\delta^2} \frac{d\delta^2}{dx}. \quad (4.10)$$

On the other hand, the orders of magnitude of the two viscoelastic terms mentioned above are

$$\frac{1}{\rho} \nabla \cdot \overline{\sigma'^{[p]} \cdot \mathbf{u}'} \sim \frac{\sigma_c^{[p]}(x)}{\rho} \left(\frac{u^*}{r^*} \right) \left[\frac{r^*}{\delta(x)} \right] \quad (4.11)$$

and

$$-\frac{1}{\rho} \overline{\sigma'^{[p]} : \nabla \mathbf{u}'} \sim \frac{\sigma_c^{[p]}(x)}{\rho} \left(\frac{u^*}{r^*} \right), \quad (4.12)$$

respectively, where u^* and r^* are the velocity and length scales associated with the interaction between the fluctuating polymer stress and the velocity gradients within the solvent. Similarly as in Guimarães *et al.* (2020) simple scaling arguments suggest that these scales are none other than the so-called Lumley (length and velocity) scales (Lumley 1973) which are defined by

$$r^* = \sqrt{\tau_p^3 \varepsilon^{[s]}} \quad (4.13)$$

and

$$u^* = \sqrt{\tau_p \varepsilon^{[s]}}, \quad (4.14)$$

respectively. Since $r^*/\delta(x)$ is a very small quantity, the viscoelastic stress power is the most important of the two viscoelastic terms in (3.3), and consequently it is the one that

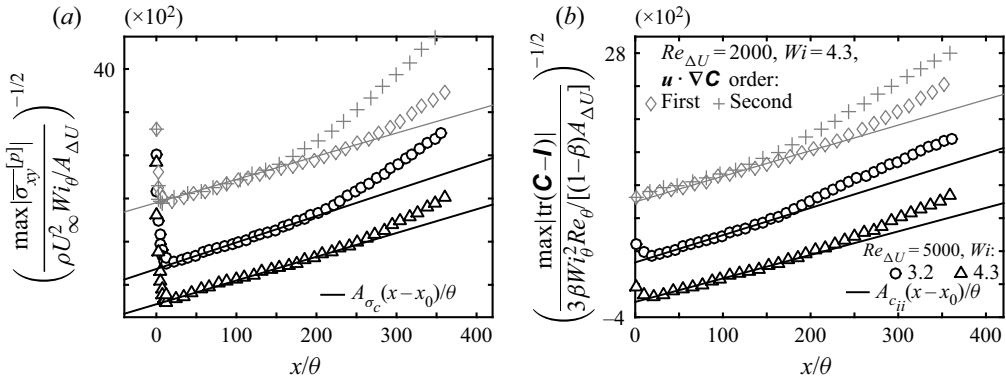


Figure 12. Streamwise evolution of (a) the maximum value of the normalised mean polymer shear stress and (b) the maximum value of the normalised averaged extension of the polymeric chains, for the simulations with $Wi = 3.2$ and 4.3 . Both evolutions are compared with the scaling relations expressed in (4.18) and (4.21). The profiles for $Wi = 4.3$ have been shifted downwards by (a) 800 units and (b) 600 units for clarity. The results from the additional simulations of Appendix B are also shown, vertically shifted by 1200 units, accessing the influence of the discretisation scheme of $\mathbf{u} \cdot \nabla \mathbf{C}$ on these quantities.

has to balance the production term, i.e.

$$-\overline{\mathbf{u}'\mathbf{u}'} : \nabla \bar{\mathbf{u}} \sim -\frac{1}{\rho} \overline{\sigma'^{[p]} : \nabla \mathbf{u}'}. \quad (4.15)$$

By using the order of magnitudes in (4.10) and (4.12), one can estimate the magnitude of $\sigma_c^{[p]}(x)$, which is

$$\sigma_c^{[p]} \sim \rho \frac{U_\infty \Delta U^2(x)}{\delta^2(x)} \frac{r^*}{u^*} \frac{d\delta^2}{dx}. \quad (4.16)$$

Substitution of the scaling laws for $\delta(x)$ and $\Delta U(x)$ in (3.1) and (3.2), into (4.16) and considering that, from the definitions of r^* and u^* , the ratio r^*/u^* is a constant given by $r^*/u^* = \tau_p$, the new scaling law for the decay of the characteristic scale of the polymer shear stress becomes

$$\frac{\sigma_c^{[p]}(x)}{\rho U_\infty^2} \sim \frac{Wi U_\infty d}{\Delta U_0 A_{\Delta U} \theta} \left(\frac{x - x_0}{\theta} \right)^{-2}. \quad (4.17)$$

By defining a Weissenberg number based on the momentum thickness $Wi_\theta = \tau_p U_\infty / \theta$, and introducing a non-dimensional scaling factor A_{σ_c} we can write

$$\left[\frac{\sigma_c^{[p]}(x)}{Wi_\theta \rho U_\infty^2 / A_{\Delta U}} \right]^{-1/2} = A_{\sigma_c} \left(\frac{x - x_0}{\theta} \right). \quad (4.18)$$

Figure 12(a) shows the streamwise evolution of $\sigma_c^{[p]}(x) = \max|\overline{\sigma_{xy}^{[p]}}(x, y)|$ for the cases with $Wi = 3.2$ and 4.3 , compared with the theoretical result expressed in (4.18). It is clear that for both cases the results from the DNS agree very well with the power law described in (4.18) for a wide range of stations x/θ . Specifically, the scaling law $\sigma_c^{[p]}(x) \sim x^{-2}$ is recovered between $20 \lesssim x/\theta \lesssim 290$ for the case with $Wi = 4.3$ and between $20 \lesssim x/\theta \lesssim 230$ for the case with $Wi = 3.2$. Unsurprisingly in both cases this power law is not observed

for very large distances from the wake origin $x/\theta \gtrsim 300$ which is consistent with the small values of $De(x)$ at these stations. Indeed, at these very large distances from the wake origin the values of the local Deborah number have decayed considerably (see § 3.2) and the assumption of large $De(x)$ is no longer valid. This can be assessed also by analysing the solvent dissipation reduction $SDR(x)$, which is a direct measure of the relative amount of turbulent energy dissipated by the polymers, which has decayed to $SDR(x) \approx 0.75$ at the end of the computational domain for $Wi = 3.2$, meaning that the influence of the molecular viscous dissipation of the solvent in (3.3) can no longer be neglected at $x/\theta \gtrsim 230$ for the case with $Wi = 3.2$. Notice, however, that the new theoretical scaling law holds for a wider region for the case with $Wi = 4.3$ than for $Wi = 3.2$ ($x/\theta \approx 270$ against $x/\theta \approx 210$), which shows that the domain of validity of the scaling law $\sigma_c^{[p]}(x) \sim x^{-2}$ increases with the inlet Weissenberg number. Appendix C discusses the evolution of a viscoelastic characteristic length $X_{elastic}$ marking the start of the decay of the viscoelastic effects in turbulent viscoelastic wakes, and thus the start of the return into a Newtonian evolution.

Another quantity of interest is the trace of \bar{C} since it is a measure of the average extension of the polymer chains and of the elastic energy stored by the polymers. If we consider the scaling relation $\bar{\sigma}^{[p]} \sim \rho v^{[p]} / \tau_p [f(\bar{C}_{kk}) \bar{C} - I]$, which is an exact result only for fluid models with an essentially constant Peterlin function (e.g. the Oldroyd-B model), and assume that the analysis given above is valid for the trace of the polymer stress tensor, we can obtain the following result:

$$\text{tr}(\bar{C} - I) \sim \frac{3\tau_p U_\infty \Delta U^2(x)}{v^{[p]} \delta^2(x)} \frac{r^*}{u^*} \frac{d\delta^2}{dx}, \tag{4.19}$$

which can be rewritten as

$$\text{tr}(\bar{C} - I) \sim \frac{3\beta}{1 - \beta} \frac{Wi^2 Re}{A_{\Delta U}} \left(\frac{d}{\theta}\right) \left(\frac{U_\infty}{\Delta U_0}\right)^2 \left(\frac{x - x_0}{\theta}\right)^{-2}, \tag{4.20}$$

where the approximation $f(\bar{C}_{kk}) \sim 1$ has been used, because it was observed that $f(\bar{C}_{kk})$ is not very different from unity for the cases considered here. As before, a scaling factor of order unity A_{cii} can also be introduced in the expression above in order to write this equation in a similar way as for $\sigma_c^{[p]}(x)$,

$$\left\{ \frac{\text{tr}(\bar{C} - I)}{3\beta Wi_\theta^2 Re_\theta / [(1 - \beta) A_{\Delta U}]} \right\}^{-1/2} = A_{cii} \left(\frac{x - x_0}{\theta}\right), \tag{4.21}$$

where $Re_\theta = U_\infty \theta / \nu^{[s]}$.

Figure 12(b) shows the streamwise evolution of $\text{tr}(\bar{C} - I)$ for the cases with $Wi = 3.2$ and 4.3, compared with the theoretical result expressed in (4.21). Clearly, there is a wide range of stations x/θ in which the power law expressed in (4.21) displays excellent agreement with the DNS results while, similarly to $\sigma_c^{[p]}(x)$, the power law is not recovered very far from the wake origin, which can be explained with the same arguments used for $\sigma_c^{[p]}(x)$. Thus, the DNS confirms the theoretical result expressed in (4.21).

Some of the results discussed in detail in Appendix B are also shown in figure 12(a,b), and evidence a slight underestimation of $[\sigma_c^{[p]}(x)]^{-2}$ and $[\text{tr}(\bar{C} - I)(x)]^{-2}$ at the far field of the wake when using a first-order discretisation scheme for $\mathbf{u} \cdot \nabla \mathbf{C}$, in comparison with a second order one, but the values of the scaling law coefficients A_{σ_c} and A_{cii} are unaffected by the choice of the numerical method employed.

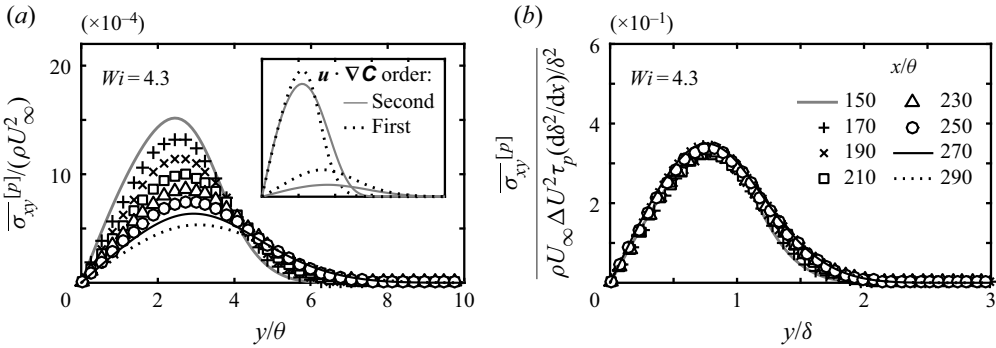


Figure 13. Transverse profiles of mean polymer shear stress $\overline{\sigma}_{xy}^{|p|}(x, y)$ for the simulation with $Wi = 4.3$ normalised by ρU_∞^2 (a) and by $\sigma_c^{|p|}$, the characteristic scale of the polymer shear stress as derived in expression (4.16) (b). The inset shows the influence of the discretisation scheme of $\mathbf{u} \cdot \nabla \mathbf{C}$ for the additional simulations discussed in Appendix B.

The fact that $\sigma_c^{|p|}(x)$ is the characteristic scale of the mean polymer shear stress $\overline{\sigma}_{xy}^{|p|}(x, y)$, as implied in the discussion leading to (4.16), is confirmed by the self-similarity of the transverse profiles of $\overline{\sigma}_{xy}^{|p|}(x, y)$ for the DNS with $Wi = 4.3$. This is demonstrated in figure 13 that shows profiles of the mean polymer shear stress without a particular normalisation (figure 13a) and normalised by $\sigma_c^{|p|}(x)$ (figure 13b). As expected, there is a considerable decay and spreading of the profiles of $\overline{\sigma}_{xy}^{|p|}/(\rho U_\infty^2)$ vs y/θ , as the flow evolves downstream (figure 13a), however, when the mean polymer shear stress is normalised by $\sigma_c^{|p|}(x)$ all the profiles collapse into the same curve (figure 13b). A similar result is observed for the other high Weissenberg number case ($Wi = 3.2$) (not shown).

Similarly, the results displayed in figure 14 attest that the characteristic scale of the polymer extension $\text{tr}(\overline{\mathbf{C}} - \mathbf{I})$ is the one expressed in (4.19) described above. The figures show transverse mean profiles of $\text{tr}(\overline{\mathbf{C}} - \mathbf{I})$ for the simulation with highest Weissenberg number ($Wi = 4.3$) using different normalisations. When no normalisation is employed the mean profiles of the polymer extension spread and decay as the flow evolves in the streamwise direction (figure 14a), however, when the same profiles are normalised with the characteristic scale of the polymer extension from (4.19) the profiles collapse into a single curve (figure 14b). The collapse is slightly less impressive for the case with $Wi = 3.2$ (not shown) but is excellent for the case with $Wi = 4.3$, which is consistent with the size of the self-similar region obtained in these cases: whereas for $Wi = 3.2$ self-similarity of the normalised mean polymer extension profiles is observed for $130 \lesssim x/\theta \lesssim 190$, it extends into the region between $130 \lesssim x/\theta \lesssim 230$ for the case with $Wi = 4.3$.

The insets of figures 13(a) and 14(a) show comparisons between profiles obtained from the simulations with lower Re that are discussed in detail in Appendix B that use first- or second-order discretisation for the $\mathbf{u} \cdot \nabla \mathbf{C}$ advection term. Overestimation is obtained with first order but the same qualitative trends are observed when using either one of the discretisation schemes.

In summary, the new theoretical results derived in this section, establishing the similarity laws governing the polymer conformation tensor and the polymer shear stress, are indeed well supported from the present DNS. The next section addresses the similarity of the Reynolds shear stresses.

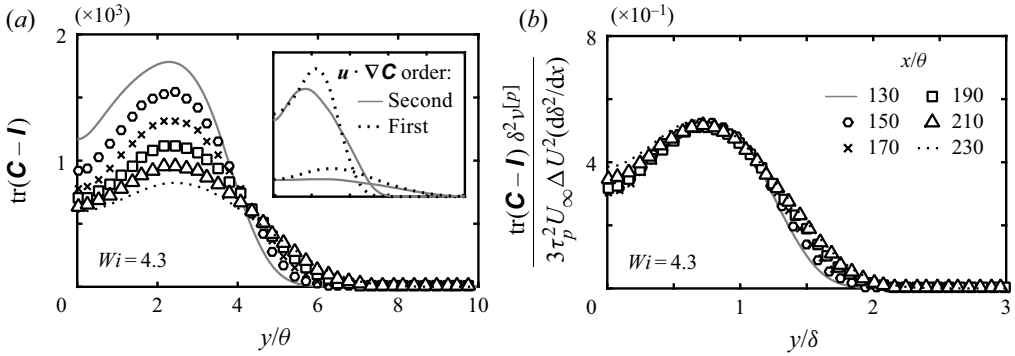


Figure 14. Transverse profiles of mean extension of the polymer chains $\text{tr}(\bar{\mathbf{C}} - \mathbf{I})$ for the simulation with $Wi = 4.3$ with no normalisation (a) and normalised using the characteristic scale derived in expression (4.19) (b). The inset shows the influence of the discretisation scheme of $\mathbf{u} \cdot \nabla \mathbf{C}$ for the additional simulations discussed in Appendix B.

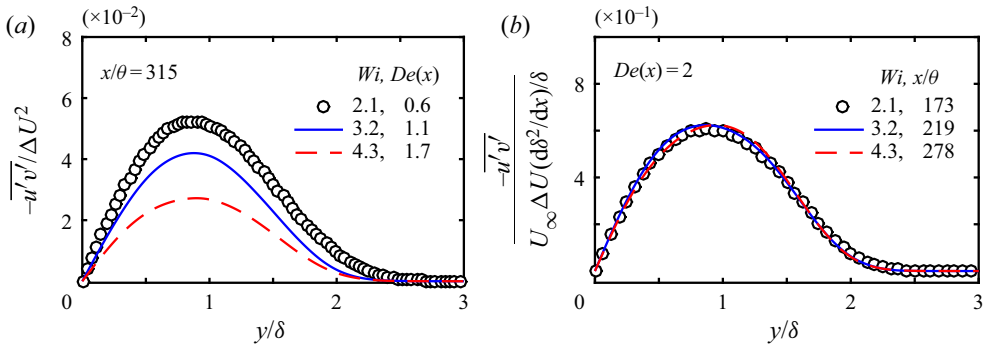


Figure 15. Transverse profiles of Reynolds shear stresses $\overline{u'v'}$ from the DNS with $Wi = 2.1, 3.2$ and 4.3 : (a) at the same station $x/\theta = 315$ (and with different values of local $De(x)$) normalised according to the classical theory for turbulent (Newtonian) wakes; (b) with the same value of the local $De(x) = 2$ (so at different stations x/θ) and normalised as in (4.23).

4.4. Similarity laws for the Reynolds shear stress

We now turn into the self-similarity of the Reynolds shear stress $\overline{u'v'}$ in turbulent viscoelastic wakes, a problem that has been addressed before for viscoelastic turbulent jets by Guimarães *et al.* (2020). We start by noting that the classical scaling used for Newtonian wakes does not lead to self-similarity of the Reynolds shear stresses in turbulent viscoelastic wakes. This can be appreciated in figure 15(a) which shows profiles of $\overline{u'v'}(x, y)/\Delta U^2(x)$, i.e. using the classical (Newtonian) scaling, for different simulations at the same location $x/\theta = 315$. Clearly, the profiles of $\overline{u'v'}/\Delta U^2(x)$ do not collapse into the same curve.

The lack of similarity for the $\overline{u'v'}(x, y)/\Delta U^2(x)$ profiles of the viscoelastic wake described above can be explained by analysing the x momentum equation, which, after a first integration can be written as

$$\frac{\overline{u'v'}(x, y)}{\Delta U^2} = \frac{1}{\delta} \frac{d\delta^2}{dx} \left\{ \int_0^\xi \frac{\psi^2(\tilde{\xi})}{2} d\tilde{\xi} \right\} - \frac{U_\infty}{\Delta U} \frac{1}{\delta} \frac{d\delta^2}{dx} \left\{ \frac{\xi \psi(\xi)}{2} \right\} + \frac{1}{\rho} \frac{\sigma_c^{[p]}}{\Delta U^2} \{\varphi(\xi)\}, \quad (4.22)$$

where $\varphi(\xi) = \overline{\sigma_{xy}^{[p]}}(x, y)/\sigma_c^{[p]}(x)$ and $\sigma_c^{[p]}(x) = \max|\overline{\sigma_{xy}^{[p]}}(x, y)|$, as defined in § 4.3. Notice that all the terms inside curly brackets ‘{ }’ on (4.22) are $O(1)$ functions of ξ only, and do not vary with either x or Wi . Note also that $U_\infty/(\Delta U\delta)$ is constant because of the momentum integral constraint (4.6). Moreover, for wakes with small velocity deficits, $U_\infty/\Delta U(x) \gg 1$, therefore the first term on the right-hand side of (4.22) is negligible compared with the second term. It follows that the lack of similarity of the profiles of $\overline{u'v'}(x, y)/\Delta U^2(x)$ can be explained by variations of the values of the spreading rate $d\delta^2/dx$ or by variations of the normalised maximum polymer shear stress $\sigma_c^{[p]}(x)/(\rho\Delta U(x)^2)$. The normalised maximum polymer shear stress, on the other hand, varies along the flow domain, as shown by the scaling derived in § 4.3 where we obtained $\sigma_c^{[p]}(x)/(\rho\Delta U(x)^2) \sim x^{-1}$.

The self-similarity condition for the Reynolds shear stresses in the turbulent viscoelastic wake can be obtained by using the large Deborah number scaling relations described in § 4.3. Specifically, by introducing (4.16) into (4.22) we can rewrite it as

$$\frac{\overline{u'v'}(x, y)}{U_\infty\Delta U(d\delta^2/dx)/\delta} = \frac{\Delta U(x)}{U_\infty} \left\{ \int_0^\xi \frac{\psi^2(\tilde{\xi})}{2} d\tilde{\xi} \right\} - \left\{ \frac{\xi\psi(\xi)}{2} \right\} + De(x)\{\varphi(\xi)\}, \quad (4.23)$$

where the scaling factor in expression (4.16) has been omitted for simplicity. Self-similar profiles of Reynolds shear stresses are recovered, for any given value of the local Deborah number $De(x)$, when normalising these profiles by $U_\infty\Delta U(x)(d\delta^2/dx)/\delta(x)$, by considering turbulent viscoelastic wakes with small velocity deficits. It is noteworthy that the scaling of the Reynolds shear stresses given by (4.23) has already been considered in George & Arndt (1989) for turbulent planar wakes of Newtonian fluids, and has been shown to provide a more universal character for the similarity of the profiles of normalised Reynolds shear stresses, because the influence of initial conditions on the spreading rate is absorbed into the scaling variables.

Equation (4.23) shows that the local Deborah number $De(x)$ appears as a new ‘equilibrium’ parameter for the viscoelastic wake, in the sense that it defines families of Reynolds shear stresses profiles. Since $De(x)$ decays in the downstream direction, it is not possible to obtain complete similarity of the Reynolds shear stresses in this flow configuration unless at regions where $De(x)$ is so small that viscoelastic effects are no longer important. This is consistent with the physical idea that self-preservation is only possible in a flow with only one characteristic (velocity and length) scale. The introduction of the Lumley scales u^* and r^* described in § 4.3 and the corresponding time scale $\tau_p = r^*/u^*$ – which is a measure of the fading memory of the viscoelastic solution – in addition to the time scale $\delta/\Delta U$, precludes the possibility of complete similarity for the viscoelastic turbulent wake, unless in the limits of $De(x) \rightarrow 0$ and possibly also $De(x) \rightarrow \infty$, where the mechanism associated with one of the two different time scales dominates the flow dynamics.

Figure 15(b) shows the profiles of Reynolds shear stresses for the simulations with $Wi = 2.1, 3.2$ and 4.3 at different stations x/θ where the local Deborah number has been fixed to $De(x) = 2$. All the Reynolds shear stress profiles collapse into the same curve when normalised by $U_\infty\Delta U(x)(d\delta^2/dx)/\delta(x)$.

5. Conclusions

This work focuses on the far field fully developed region of turbulent viscoelastic planar wakes. The work is based on spatially developing DNS carried out with a high-order code

that has been used by the authors in similar investigations of turbulent viscoelastic planar jets, that employs the FENE-P rheological model (Guimarães *et al.* 2020).

The DNS show that increasing the value of the inlet Weissenberg number results in a strong attenuation of the Reynolds stresses, viscous dissipation rate of the solvent, and of the spreading and velocity deficit decay rates in the far field of the wake, in agreement with results from previous experimental studies (Pokryvailo *et al.* 1973; Borisov *et al.* 1990; Pinho & Whitelaw 1991; Cressman *et al.* 2001). However, in the distant far-field region the viscoelastic effects die out and the turbulent wake statistics show a clear tendency to approach the corresponding Newtonian values. This return to Newtonian tendency is explained by the drastic decrease of the local Deborah number at the distant far-field regions of the wake, and the extent of the initial far-field region where viscoelastic effects are strong increases with the inlet Weissenberg number Wi .

A new theory was developed to describe the far-field of turbulent planar wakes with viscoelastic fluids. The theory is based on the thin shear layer approximation and on a similarity analysis of the equations governing the fluid motion and identifies the reference length and time scales characterising turbulent wakes of viscoelastic fluids, which explains the self-similarity of the profiles of mean velocity, mean polymer shear stress, averaged polymer chain extension and the conditions for similarity of the Reynolds shear stress, which is observed in results from the simulations. Scaling laws for the wake shear layer thickness and mean velocity deficit have been derived yielding $\delta(x) \sim x^{1/2}$ and $\Delta U(x) \sim x^{-1/2}$, respectively. Additionally, scaling relations have been derived for maximum polymer shear stresses and averaged polymer chain extension decay, $\sigma_c^{[p]} \sim x^{-2}$ and $\text{tr}(\bar{C} - I) \sim x^{-2}$, respectively. All the new theoretical results display excellent agreement with the results from the DNS.

As in Guimarães *et al.* (2020) the new theoretical results described here have been based on classical similarity analysis and simple scaling arguments, supplied with the theory of Lumley (1973) to describe viscoelastic turbulent flows. Therefore, a similar approach can probably be used to describe the far-field of other free turbulent flows with viscoelastic fluids such as turbulent jets and wakes in axisymmetric configuration, as well as mixing layers.

Acknowledgements. The authors are grateful to Professor K. Horiuti for interesting discussions on turbulence for viscoelastic fluids.

Funding. M.C.G. acknowledges Fundação para a Ciência e Tecnologia (FCT) through contract UIBD/151060/2021. C.B.S. acknowledges Fundação para a Ciência e Tecnologia (FCT) through IDMEC, under LAETA, project UIDB/50022/2020., and projects PCIF/GFC/0109/2017 and PCIF/MPG/0147/2019. F.T.P. is thankful for funding by FCT and Centro de Estudos de Fenómenos de Transporte through projects UIDB/00532/2020 and UIDP/00532/2020. F.T.P. is thankful for funding by FCT and ALiCE through project LA/P/0045/2020.

Declaration of interests. The authors report no conflict of interest.

Author ORCIDiDs.

- ① Mateus C. Guimarães <https://orcid.org/0000-0001-6268-3968>;
- ① Fernando T. Pinho <https://orcid.org/0000-0002-9576-4622>;
- ① Carlos B. da Silva <https://orcid.org/0000-0002-6866-5469>.

Appendix A. Assessment of the lateral sizes L_y and L_z used in the simulations

As described in § 2.3 the present work uses DNS of turbulent viscoelastic wakes carried out in a computational domain which is very long in the streamwise direction ($L_x = 84d$) while the size of the lateral dimension remains comparatively small ($L_y = 24d$). For this

reason, and given the fact that the present numerical scheme employs periodic boundary conditions along this (lateral) direction, it is important to demonstrate that in all cases the lateral boundary conditions are placed sufficiently far away from the turbulent core region of the wake in order to avoid any undesirable confinement effects.

For this purpose we compared results from three additional (Newtonian) DNS using different values of L_y/d , and correspondingly different number of grid points in this direction N_y , so that the grid size $\Delta y/d$ was kept constant and equal in all cases. Specifically, we carried out DNS using lateral domain lengths of $L_y = 16d, 24d$, and $48d$, for a total number of grid points (in the y direction) equal to $N_y = 512, 768$ and 1536 , respectively, while the number of points in the remaining directions is $N_x = 2688$ and $N_z = 192$ and the size of the computational domain in these directions is the same as before, i.e. $L_x = 84d$ and $L_z = 6d$. The decrease in the number of points in these (streamwise and spanwise) directions was imposed by the very high computational cost of the simulations, and naturally imposed restrictions in the Reynolds number of these simulations. Whereas in the core of the article the Reynolds number used was set to $Re_{\Delta U} = 5000$ (and $Re = 14\,286$) for a Taylor based Reynolds number of $Re_\lambda \approx 100$, in the simulations used in this Appendix we limited these Reynolds numbers to $Re_{\Delta U} = 2000$ ($Re \approx 5714$) and $Re_\lambda \approx 70$, while the resolution approaches $\Delta x/\eta_{42d} \approx 2$. All remaining numerical and physical parameters were the same as those described at § 2. The assessment of the lateral boundary conditions was investigated using Newtonian cases because these lead to higher spreading rates than in viscoelastic wakes and consequently are more useful to investigate the possible existence of lateral confinement effects.

Figure 16 shows the streamwise (x) evolution of several classical statistics obtained in these four new DNS of Newtonian turbulent wakes. The results obtained with different values of L_y/d are almost indistinguishable, confirming that $L_y/d = 24$ is indeed appropriate for the lateral size of the computational domain. In fact, the figures indicate that $L_y/d = 16$ would be already sufficiently large. Additionally, it can be seen that the influence of the Reynolds number on the flow statistics is only quantitative, and in any case very mild, at least for the normalised first- and second-order moments of velocity and for the viscous dissipation rate. This suggests that the Reynolds number chosen for the DNS used in the present work is sufficiently high, however, the final confirmation can only be gained when comparing the present numerical results with the available literature data, as shown next.

Figure 17 shows transverse profiles of the mean velocity deficit, and of the Reynolds stresses for the four Newtonian DNS, compared with the experimental and numerical results obtained by Townsend (1949), Ueberoi & Freymuth (1969), Narasimha & Prabhu (1972), Browne & Antonia (1986), Wignanski *et al.* (1986), Weygant & Mehta (1989), Aronson & Löfdahl (1993), Zhou & Antonia (1995), Moser *et al.* (1999), Schenck & Jovanovic (2002), Hickey *et al.* (2013) and Tang *et al.* (2016).

The mean profile of the velocity deficit is virtually the same in all the numerical and experimental data available (figure 17e), and differences can be observed only in the profiles of the Reynolds stresses (figure 17a–d). It is noteworthy that the curves corresponding to the DNS discussed in this Appendix (with different domain sizes and Reynolds numbers) and the curves for the reference Newtonian DNS used in the present work, are all virtually equal. This again confirms that (i) the domain lateral size L_y used in the present DNS has no influence on the results and (ii) the Reynolds numbers used in all the present DNS is sufficiently high to attain the far-field fully developed (self-similar) region of the wake.

The observed differences between the present DNS and the various experimental and numerical data in the literature are smaller than the differences observed between the

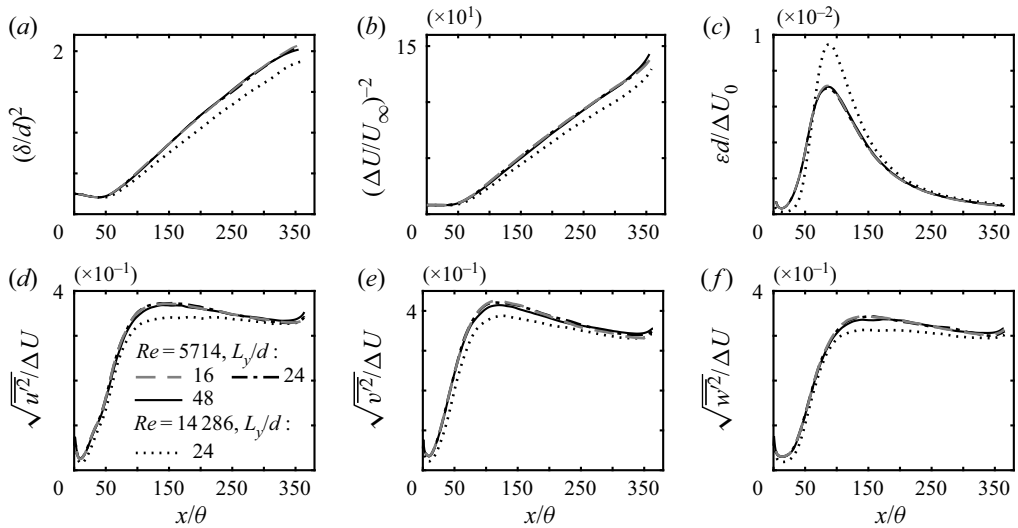


Figure 16. Streamwise evolution of several statistics from the three Newtonian turbulent wakes with different computational domain heights L_y/d , and different Reynolds numbers (see inset in panel (d) for details): (a) wake half-widths; (b) wake velocity deficits; (c) viscous dissipation rate; (d–f) normal Reynolds stresses.

literature data themselves. This confirms the well known lack of universality of the turbulent wake statistics caused by the different initial/inlet conditions available in each experiment/simulation. Nevertheless, the profiles show that the results from the present DNS are in general agreement with the data previously obtained by different authors, which again validates the present DNS.

We have carried out one extra (new) simulation with $L_z/d = 12$, i.e. using a domain width that is two times larger than that of the other simulations, while keeping the same resolution as before by increasing the number of grid points by a factor of two in that direction ($N_z = 576$ instead of $N_z = 288$). The new simulation uses the full second-order Kurganov–Tadmor scheme and a Weissenberg number of $Wi = 4.3$. The case with the largest Wi was selected because the structures are typically larger in the spanwise direction when Wi is high. Figure 18 shows this new simulation ($L_z/d = 12$) together with an additional comparison regarding the discretisation scheme of the advection term of the conformation tensor, to be discussed in Appendix B. Virtually no differences are found between the statistics obtained from the cases with $L_z = 6d$ and $L_z = 12d$, attesting that $L_z = 6d$ is already sufficiently large for all the simulations presented in this work.

Appendix B. Assessment of the simplification used in computation of the advection term of the conformation tensor

In this Appendix we assess the influence of the discretisation scheme for the advection term of the conformation tensor evolution equation (first- or second-order Kurganov–Tadmor scheme) as discussed in the main text of the paper (§ 2.2). To assess this we compare the results of two new (additional) DNS of turbulent viscoelastic wakes with the highest Wi number used in the present work ($Wi = 4.3$). The additional simulations use $\beta = 0.8$ and $L^2 = 100^2$ for the remaining rheological parameters, while the lateral domain size is $L_y/d = 16$ and differs only on the numerical scheme used to compute the advection term in the conformation tensor transport equation. While in one simulation the

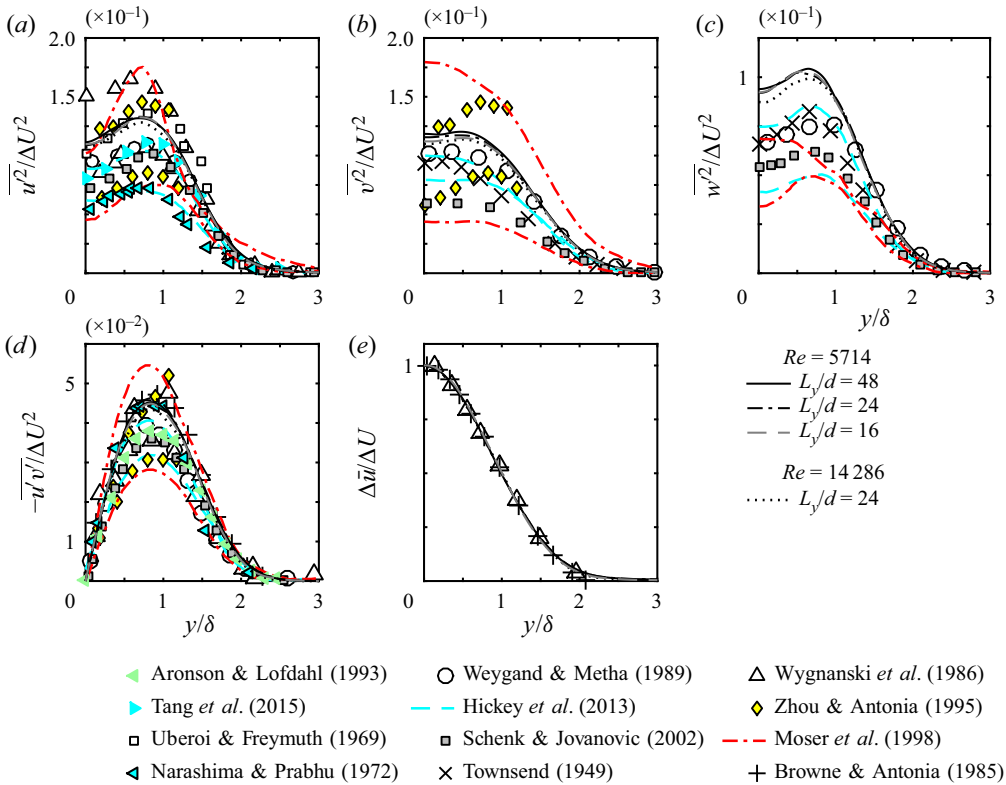


Figure 17. Profiles of the Reynolds stress and mean velocity deficit at the far-field region for the three Newtonian planar wakes discussed in this Appendix, using different inlet conditions, normalised with the classical theory. The results are compared also with the numerical and experimental data available from the literature (described in the main text), and with the reference Newtonian DNS used in the present work.

Kurganov–Tadmor scheme is used in a first-order configuration the other simulation uses a second-order Kurganov–Tadmor scheme for this purpose. Two cases with the highest Wi used in this work have been chosen because the advection term is a dominant term of the C_{ij} equation when Wi is large, and so larger differences are to be expected in these cases. The results are also compared with one of the Newtonian simulations described above (in Appendix A) with $L_y/d = 16$, and a viscoelastic simulation with a larger spanwise domain width $L_z/d = 12$.

The comparison between several turbulent wake statistics is shown in figure 18, and includes the streamwise evolution of the integral wake parameters, and of the Reynolds stresses, as well as the mean values of the components of C_{ij} . It is clear that the evolution of the integral wake parameters, i.e. $\delta(x)$ and $\Delta U(x)$ is virtually equal in the two viscoelastic simulations, and even the Reynolds stresses display mild quantitative differences that do not alter in any way the conclusions of this study. Specifically, both viscoelastic simulations display drastic decrease of the spreading and velocity deficit decaying rates compared with the Newtonian case, at regions where $De(x)$ is large, and the subsequent attenuation of these viscoelastic effects when $De(x)$ has decayed, regardless of the choice for the numerical scheme for the advection term of C_{ij} . Regarding the evolution of the mean conformation tensor components, figure 18 shows that the differences between the components of C_{ij} obtained with the two numerical schemes are actually very small once

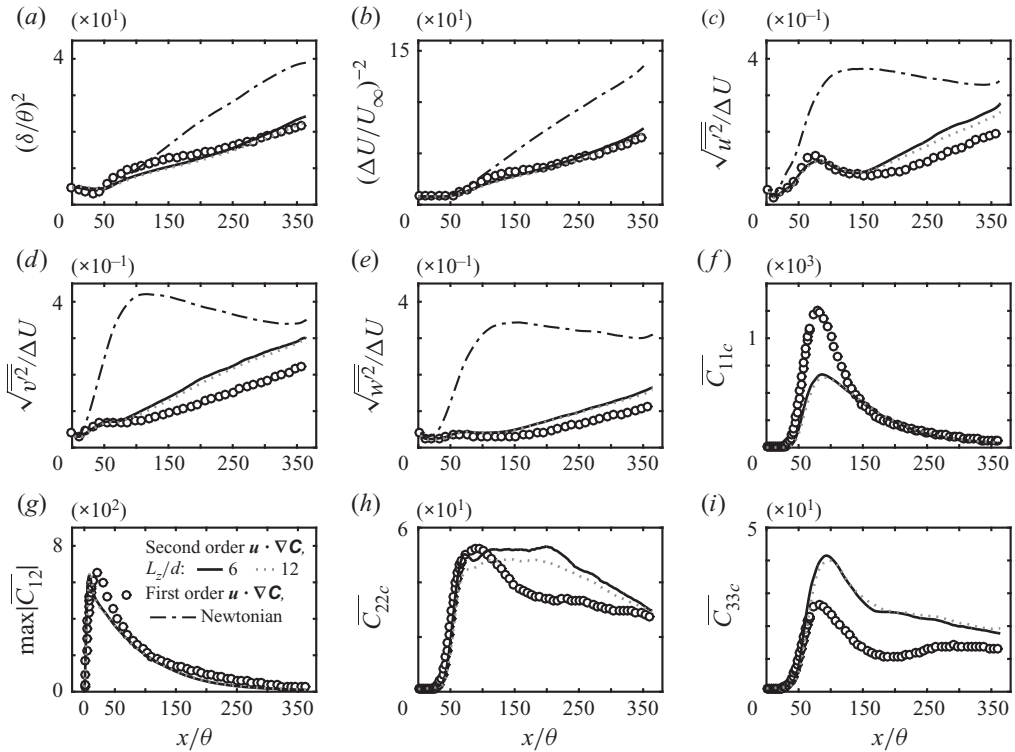


Figure 18. Streamwise evolution of several turbulence statistics from three DNS of turbulent viscoelastic wakes (for Weissenberg number $Wi = 4.3$) carried out with different numerical schemes for the advection term of the conformation tensor transport equation and different domain widths L_z . The results from one Newtonian turbulent wake are also shown for comparison: (a) wake half-width; (b) wake velocity deficit; (c–e) square root of the normal Reynolds stresses; (f–i) mean conformation tensor components (see inset in panel(g) for details).

an intermediate region of the flow has been crossed, i.e. differences are small at the far-field. For instance, larger differences in \overline{C}_{11} are obtained at a small portion of the domain, at the transition region where velocity gradients are more intense, but similar values are obtained at the far-field. For the \overline{C}_{12} component, the differences are small everywhere and for \overline{C}_{22} and \overline{C}_{33} the same qualitative trend can be observed. Thus one concludes that the differences between the results obtained using the original method for computing the advection term of the conformation tensor (as used in Guimarães *et al.* (2020)) and the one used here are very small and do not affect the results and conclusions of the present work.

Appendix C. The viscoelastic characteristic length, $X_{elastic}$

The results from the present simulations show that turbulent viscoelastic wakes, although exhibiting different characteristics than the classical (Newtonian) turbulent wakes, will eventually revert to the Newtonian evolution laws, for example the wake spreading rate, provided a sufficient large distance from the wake origin is attained. This Appendix discusses a possible method to estimate the viscoelastic characteristic length $X_{elastic}$, as measured from the wake origin, where strong viscoelastic effects cease to be observed, thereby implying a recovery of the Newtonian wake characteristics. We define $X_{elastic}$ as

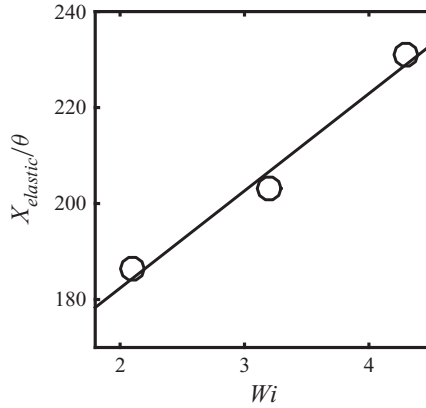


Figure 19. Viscoelastic characteristic length $X_{elastic}$, marking the start of the return to a Newtonian spreading rate, i.e. the end of the flow region where a strong spreading rate reduction caused by viscoelasticity can be observed in turbulent viscoelastic wakes.

the coordinate in the streamwise direction where the reduction of the viscoelastic effects starts, so that by $x \gg X_{elastic}$ the wake statistics are similar to the typical Newtonian values. We focus on the simplest integral quantity – the wake half-width $\delta(x)$ – and compute $X_{elastic}$ using the following method. For each curve of $(\delta(x)/\theta)^2$ with $Wi \geq 2.1$ shown in figure 2 we obtain two best fit lines at two different regions of the flow: the first far-field region where the spreading rate is reduced by the viscoelasticity; and the second far-field region where it has a value close to Newtonian. The non-dimensional distance $X_{elastic}/\theta$ is obtained from the interception of these two lines.

The results are shown in figure 19, where an approximately linear dependence with Wi can be observed. This linear dependence can be justified using the following scaling arguments. Since the definition of $\delta(x)$ is based on the mean velocity \bar{u} , it is natural to consider the x momentum equation for an estimate of $X_{elastic}$. We assume that at $x = X_{elastic}$ viscoelastic effects are still important so that the viscoelastic term is of the same order of the turbulent stress term, i.e. $\rho^{-1} \partial \overline{\sigma_{xy}^{[p]}} / \partial y \sim \partial \overline{u'v'} / \partial y$. Notice that this is not valid for all x stations but only at the vicinity of $x = X_{elastic}$. Using the scaling relations for the polymer and turbulent stresses that have been derived in § 4.3, and taking $x = X_{elastic}$ leads to

$$\frac{Wi U_\infty^3 d[(X_{elastic} - X_0)/\theta]^{-5/2}}{\theta^2 \Delta U_0 A_\delta^{1/2} A_{\Delta U}} \sim \frac{U_\infty^2 A_\delta^{1/2} [(X_{elastic} - X_0)/\theta]^{-3/2}}{\theta A_{\Delta U}}, \quad (C1)$$

and by introducing a proportionality constant α and solving for $X_{elastic}$ we can write

$$\frac{X_{elastic}}{\theta} = \alpha Wi + \frac{X_0}{\theta}, \quad (C2)$$

where the scaling law coefficients in (C1) have been absorbed by the constant α , and where we have also replaced Wi_θ by Wi without loss of generality (X_0 is a virtual origin for this law). It is plausible that $X_{elastic}$ is also a function of other rheological and flow parameters such as L , β and Re . Presently, only the dependence with Wi has been considered and we must stress that this expression is not applicable to flows with low Wi as no spreading rate reduction is observed for these cases.

REFERENCES

- ABREU, H., PINHO, F.T. & DA SILVA, C.B. 2022 Turbulent entrainment in viscoelastic fluids. *J. Fluid Mech.* **934**, A26.
- ARONSON, D. & LÖFDAHL, L. 1993 The plane wake of a cylinder: measurements and inferences on turbulence modeling. *Phys. Fluids A* **5** (6), 1433–1437.
- AZAIÉZ, J. & HOMS, G.M. 1994 Linear stability of free shear flow of viscoelastic liquids. *J. Fluid Mech.* **268**, 37–69.
- BIRD, R.B., DOTSON, P.J. & JOHNSON, N.L. 1980 Polymer solution rheology based on a finitely extensible bead-spring chain model. *J. Non-Newtonian Fluid Mech.* **7**, 213–235.
- BORISOV, A.N., MIRONOV, B.P., NOVIKOV, B.G. & FEDOSENKO, V.D. 1990 Wake flows in dilute polymer solutions. In *Structure of Turbulence and Drag Reduction* (ed. A. Gyr), pp. 249–255. Springer.
- BROWNE, L.W.B. & ANTONIA, R.A. 1986 Reynolds shear stress and heat flux measurements in a cylinder wake. *Phys. Fluids* **29** (3), 709–713.
- CADOT, O. & KUMAR, S. 2000 Experimental characterization of viscoelastic effects on two- and three-dimensional shear instabilities. *J. Fluid Mech.* **416**, 151–172.
- CANUTO, C., HUSSAINI, M.Y., QUARTERONI, A. & ZANG, T.A. 1987 *Spectral Methods in Fluid Dynamics*. Springer.
- COELHO, P.M. & PINHO, F.T. 2003a Vortex shedding in cylinder flow of shear-thinning fluids: I. Identification and demarcation of flow regimes. *J. Non-Newtonian Fluid Mech.* **110** (2–3), 143–176.
- COELHO, P.M. & PINHO, F.T. 2003b Vortex shedding in cylinder flow of shear-thinning fluids. II. Flow characteristics. *J. Non-Newtonian Fluid Mech.* **110** (2–3), 177–193.
- COELHO, P.M. & PINHO, F.T. 2004 Vortex shedding in cylinder flow of shear-thinning fluids. III. Pressure measurements. *J. Non-Newtonian Fluid Mech.* **121** (1), 55–68.
- CRESSMAN, J.R., BAILEY, Q. & GOLDBURG, W.I. 2001 Modification of a vortex street by a polymer additive. *Phys. Fluids* **13** (4), 867–871.
- FERREIRA, P.O., DA SILVA, C.B. & PINHO, F.T. 2016 Large-eddy simulations of forced isotropic turbulence with viscoelastic fluids described by the FENE-P model. *Phys. Fluids* **28** (12), 125104.
- GADD, G.E. 1966 Effects of long-chain molecule additives in water on vortex streets. *Nature* **211**, 169–170.
- GEORGE, W.K. 2008 Is there an asymptotic effect of initial and upstream conditions on turbulence? In *Fluids Engineering Division Summer Meeting*, vol. 48418, pp. 647–672.
- GEORGE, W.K. 1989 The self-preservation of turbulent flows and its relation to initial conditions and coherent structure. In *Advances in Turbulence* (ed. W.K. George & R. Arndt), pp. 39–73. Hemisphere.
- GUIMARÃES, M.C., PIMENTEL, N., PINHO, F.T. & DA SILVA, C.B. 2020 Direct numerical simulations of turbulent viscoelastic jets. *J. Fluid Mech.* **899**, A11.
- HICKEY, J.P., HUSSAIN, F. & WU, X. 2013 Role of coherent structures in multiple self-similar states of turbulent planar wakes. *J. Fluid Mech.* **731**, 312–363.
- HORIUTI, K., MATSUMOTO, K. & FUJIWARA, K. 2013 Remarkable drag reduction in non-affine viscoelastic turbulent flows. *Phys. Fluids* **25**, 015106.
- KATO, H. & MIZUNO, Y. 1983 An experimental investigation of viscoelastic flow past a circular cylinder. *Bull. JSME* **26** (214), 529–536.
- KIM, J. & MOIN, P. 1985 Application of a fractional-step method to incompressible Navier–Stokes equations. *J. Comput. Phys.* **59**, 308–323.
- KIM, K., LI, C., SURESHKUMAR, R., BALACHANDAR, S. & ADRIAN, R.J. 2007 Effects of polymer stresses on eddy structures in drag-reduced turbulent channel flow. *J. Fluid Mech.* **584**, 281–299.
- KURGANOV, A. & TADMOR, E. 2000 New high-resolution central schemes for nonlinear conservation laws and convection-diffusion equations. *J. Comput. Phys.* **160** (1), 241–282.
- LELE, S.K. 1992 Compact finite difference schemes with spectral-like resolution. *J. Comput. Phys.* **103**, 16–42.
- LIU, X., THOMAS, F.O. & NELSON, R.C. 2002 An experimental investigation of the planar turbulent wake in constant pressure gradient. *Phys. Fluids* **14** (8), 2817–2838.
- LUMLEY, J.L. 1973 Drag reduction in turbulent flow by polymer additives. *J. Polym. Sci.* **7** (1), 263–290.
- METZNER, A.B. & METZNER, A.P. 1970 Stress levels in rapid extensional flows of polymeric fluids. *Rheol. Acta.* **9** (2), 174–181.
- MICHALKE, A. 1965 On spatially growing disturbances in an inviscid shear layer. *J. Fluid Mech.* **23**, 521–544.
- MONKEWITZ, P.A. & HUERRE, P. 1982 Influence of the velocity ratio on the spatial instability of mixing. *Phys. Fluids* **25** (7), 1137–1143.
- MOSER, R.D., KIM, J. & MANSOUR, N.N. 1999 Direct numerical simulation of turbulent channel flow up to $Re_\tau = 590$. *Phys. Fluids* **11** (4), 943–945.

- MOSER, R.D., ROGERS, M.M. & EWING, D.W. 1998 Self-similarity of time-evolving plane wakes. *J. Fluid Mech.* **367**, 255–289.
- NARASIMHA, R. & PRABHU, A. 1972 Equilibrium and relaxation in turbulent wakes. *J. Fluid Mech.* **54** (1), 1–17.
- ORLANSKI, I. 1976 A simple boundary condition for unbounded hyperbolic flows. *J. Comput. Phys.* **21** (3), 251–269.
- PARVAR, S., DA SILVA, C.B. & PINHO, F.T. 2020 Local similarity solution for steady laminar planar jet flow of viscoelastic fene-p fluids. *J. Non-Newtonian Fluid Mech.* **279**, 104265.
- PERLEKAR, P., MITRA, D. & PANDIT, R. 2010 Direct numerical simulations of statistically steady, homogeneous, isotropic fluid turbulence with polymer additives. *Phys. Rev. E* **82**, 66313.
- PINHO, F.T. & WHITELAW, J.H. 1991 Flow of non-Newtonian fluids over a confined baffle. *J. Fluid Mech.* **226**, 475–496.
- POKRYVAILO, N.A., SHUL'MAN, Z.P., SOBOLEVSKII, A.S., PROKOPCHUK, D.A., KOVALEVSKAYA, N.D., PASHIK, G.M., TOVCHIGRECHKO, V.V. & ZHDANOVICH, N.V. 1973 Flow of polymer solutions in wakes of poorly streamlined bodies. *J. Engng Phys.* **25** (6), 1488–1492.
- POPE, S.B. 2000 *Turbulent Flows*. Cambridge University Press.
- POT, P.J. 1979 Measurements in a 2-D wake and in a 2-D wake merging into boundary layer: data report. *Tech. Rep. NLR-TR 79063* U. National Aerospace Laboratory.
- RAMAPRIAN, B.R. 1984 Study of large-scale mixing in developing wakes behind streamlined bodies. *Tech. Rep. CR-173478*. NASA.
- RICHTER, D., IACCARINO, G. & SHAQFEH, E.S.G. 2012 Effects of viscoelasticity in the high Reynolds number cylinder wake. *J. Fluid Mech.* **693**, 297–318.
- RICHTER, D., SHAQFEH, E.S.G. & IACCARINO, G. 2011 Floquet stability analysis of viscoelastic flow over a cylinder. *J. Non-Newtonian Fluid Mech.* **166** (11), 554–565.
- SARPKAYA, T., RAINEY, P.G. & KELL, R.E. 1973 Flow of dilute polymer solutions about circular cylinders. *J. Fluid Mech.* **57** (1), 177–208.
- SCHENCK, T. & JOVANOVIĆ, J. 2002 Measurement of the instantaneous velocity gradients in plane and axisymmetric turbulent wake flows. *J. Fluids Engng* **124** (1), 143–153.
- SCHLICHTING, H. 1930 Über das ebene Windschattenproblem. *Ing.-Arch.* **1** (5), 533–571.
- SEYER, F.A. & METZNER, A.B. 1969 Turbulence phenomena in drag reducing systems. *AIChE J.* **15** (3), 426–434.
- DA SILVA, C.B., LOPES, D.C. & RAMAN, V. 2015 The effect of subgrid-scale models on the entrainment of a passive scalar in a turbulent planar jet. *J. Turbul.* **16** (4), 342–366.
- DA SILVA, C.B. & MÉTAIS, O. 2002 Vortex control of bifurcating jets: a numerical study. *Phys. Fluids* **14** (11), 3798–3819.
- STANLEY, S.T. & SARKAR, S. 1997 Simulations of spatially developing two-dimensional shear layers and jets. *Theor. Comput. Fluid Dyn.* **9** (2), 121–147.
- TANG, S.L., ANTONIA, R.A., DJENIDI, L. & ZHOU, Y. 2016 Complete self-preservation along the axis of a circular cylinder far wake. *J. Fluid Mech.* **786**, 253–274.
- TENNEKES, H. & LUMLEY, J.L. 1972 *A First Course in Turbulence*. MIT Press.
- TIRTAATMADJA, V. & SRIDHAR, T. 1993 A filament stretching device for measurement of extensional viscosity. *J. Rheol.* **37** (6), 1081–1102.
- TOWNSEND, A.A. 1949 The fully developed wake of a circular cylinder. *Aust. J. Chem.* **2** (4), 451–468.
- TOWNSEND, A.A. 1976 *The Structure of Turbulent Shear Flow*. Cambridge University Press.
- UBEROI, M.S. & FREYMUTH, P. 1969 Spectra of turbulence in wakes behind circular cylinders. *Phys. Fluids* **12** (7), 1359–1363.
- VAITHIANATHAN, T., ROBERT, A., BRASSEUR, J.G. & COLLINS, L.R. 2006 An improved algorithm for simulating three-dimensional, viscoelastic turbulence. *J. Non-Newtonian Fluid Mech.* **140** (1), 3–22.
- VALENTE, P.C., DA SILVA, C.B. & PINHO, F.T. 2014 The effect of viscoelasticity on the turbulent kinetic cascade. *J. Fluid Mech.* **760**, 39–62.
- VALENTE, P.C., DA SILVA, C.B. & PINHO, F.T. 2016 Energy spectra in elasto-inertial turbulence. *Phys. Fluids* **28**, 075108.
- VONLANTHEN, R. & MONKEWITZ, P.A. 2013 Grid turbulence in dilute polymer solutions: peo in water. *J. Fluid Mech.* **730**, 76–98.
- WATANABE, T. & GOTOH, T. 2010 Coil-stretch transition in an ensemble of polymers in isotropic turbulence. *Phys. Rev. E* **81** (6), 066301.
- WEYGANDT, J.H. & MEHTA, R.D. 1989 Asymptotic behavior of a flat plate wake. *Tech. Rep. JIAA Tr-95*. Stanford University.

- WHITE, C.M. & MUNGAL, M.G. 2008 Mechanics and prediction of turbulent drag reduction with polymer additives. *Annu. Rev. Fluid Mech.* **40**, 235–256.
- WILLIAMSON, C.H.K. 1996 Vortex dynamics in the cylinder wake. *Annu. Rev. Fluid Mech.* **28** (1), 477–539.
- WILLIAMSON, J.H. 1980 Low-storage Runge–Kutta schemes. *J. Comput. Phys.* **35**, 48–56.
- WYGNANSKI, I., CHAMPAGNE, F. & MARASLI, B. 1986 On the large-scale structures in two-dimensional, small-deficit, turbulent wakes. *J. Fluid Mech.* **168**, 31–71.
- XIONG, Y.L., BRUNEAU, C.H. & KELLAY, H. 2013 A numerical study of two dimensional flows past a bluff body for dilute polymer solutions. *J. Non-Newtonian Fluid Mech.* **196**, 8–26.
- YAMANI, S., KESHAVARZ, B., RAJ, Y., ZAKI, T.A., MCKINLEY, G.H. & BISCHOFBERGER, I. 2021 Spectral universality of elastoinertial turbulence. *Phys. Rev. Lett.* **127** (7), 074501.
- ZECCHETTO, M. & DA SILVA, C.B. 2021 Universality of small-scale motions within the turbulent/non-turbulent interface layer. *J. Fluid Mech.* **916**, A9.
- ZHOU, Y. & ANTONIA, R.A. 1995 Memory effects in a turbulent plane wake. *Exp. Fluids* **19** (2), 112–120.